HAL open science

Investigation of the multiple-fragmentation process and post-fragmentation behaviour of dense and nacre-like alumina ceramics by means of tandem impact experiments and tomographic analysis

Yannick Duplan, Pascal Forquin

▶ **To cite this version:**

Yannick Duplan, Pascal Forquin. Investigation of the multiple-fragmentation process and post-fragmentation behaviour of dense and nacre-like alumina ceramics by means of tandem impact experiments and tomographic analysis. International Journal of Impact Engineering, 2021, 155, pp.103891. 10.1016/j.ijimpeng.2021.103891 . hal-03225774

HAL Id: hal-03225774

https://hal.science/hal-03225774v1

Submitted on 24 May 2023

HAL is a multi-disciplinary open access archive for the deposit and dissemination of scientific research documents, whether they are published or not. The documents may come from teaching and research institutions in France or abroad, or from public or private research centers.

L'archive ouverte pluridisciplinaire **HAL**, est destinée au dépôt et à la diffusion de documents scientifiques de niveau recherche, publiés ou non, émanant des établissements d'enseignement et de recherche français ou étrangers, des laboratoires publics ou privés.

Distributed under a Creative Commons Attribution - NonCommercial - NoDerivatives 4.0 International License

Version of Record: https://www.sciencedirect.com/science/article/pii/S0734743X21000786
Manuscript_19f031f040dec480f2f6280f1c065d3a

Investigation of the multiple-fragmentation process and *post*-fragmentation behaviour of dense and nacre-like alumina ceramics by means of tandem impact experiments and tomographic analysis

Yannick Duplan[1], Pascal Forquin[1†]

[1] Univ. Grenoble Alpes, CNRS, Grenoble INP*, 3SR, 38000 Grenoble, France

[*] Institute of Engineering Univ. Grenoble Alpes

[†] Corresponding author: pascal.forquin@3sr-grenoble.fr

ABSTRACT

During the impact by an armour-piercing projectile against a bilayer ceramic/backing protective system, dynamic tensile stresses are generated leading to the inception and the propagation of numerous and oriented cracks. This intense tensile damage, called fragmentation, affects the performances of the shielding and its capacity to resist to multiple impact. The residual confined strength of a fragmented ceramic is relatively weak compared to its undamaged compressive strength, however not negligible. Characterising the dynamic behaviour of a pre-fragmented ceramic is then of interest to design improved armour solutions. In this work, an impact configuration called tandem test, which consists in a normal impact followed by a penetrating impact, is applied to two alumina ceramics with different microstructures: a conventional 98% pure alumina compared to a bioinspired brick-and-mortar ceramic called "MAINa" (a nacre-like alumina) which exhibits higher flexural strength and fracture-toughness. Following the normal impact tests, a fragments size analysis is conducted by means of X-ray micro-computed tomography distribution, which reveals that the mean fragments size is significantly larger in the nacre-like alumina, thus demonstrating a correlation between the fragments size and the penetrating resistance of fragmented alumina ceramic. Finally, the strength of both alumina ceramics in their fragmented state is identified

© 2021 published by Elsevier. This manuscript is made available under the CC BY NC user license
https://creativecommons.org/licenses/by-nc/4.0/

based on an inverse approach in which the penetrating tests are numerically simulated considering the Drucker-Prager model.

Keywords: *Armour, damage, X-ray tomography, fragments size, Drucker-Prager model.*

---

1 Introduction

In Vietnam War (1955 – 1975) and later on, advanced ceramics have been largely used in armour systems to create lightweight body and vehicle protection to resist against bullet projectiles, such as the well-known Armour-Piercing (AP) projectiles [1]. Alumina (Al_2O_3) ceramics are common ceramic materials used in ballistics, along with titanium diboride (TiB_2), boron carbide (B_4C) and silicon carbide (SiC). Among these four ceramics, Al_2O_3 has the lowest ballistic efficiency and the highest density, but the total cost is much lower that makes Al_2O_3 very attractive [2]. Due to their compression strength, ceramic materials are used in bilayer shielding, which constitutes among the most efficient protective configuration, to shatter and break the impacting threat of the projectile core by erosion and fragmentation [3–5]. However, ceramics exhibit *a contrario* a brittle behaviour and their inherent low tensile properties make necessary the use of a ductile plate (aluminium alloy, steel, composites such as fibre-reinforced polymer) as backing, in order to convert the debris' kinetic energy and mechanical momentum into deformation and delamination [4,6]. For instance, it was observed that the ballistic limit velocity of a 11.4-mm thick alumina plate (AD-85) was only 390 m/s compared to 650 m/s for a 6.35-mm alumina (AD-85) backed with aluminium of same thickness [7]. The impact scenario of an AP projectile against a ceramic plate can be divided into three phases [8–10]. For ~ 1 μs, a triaxial compression under uniaxial strain is generated, inducing damage mechanisms such as micro-plasticity (with pore collapse) and micro-cracking [8,11], under strain-rates exceeding 10,000 s^{-1}. In the second loading phase (1 – 5 μs), a dynamic fragmentation due to high strain-rate tensile loading occurs. Finally, the third

stage, which is the longest one (up to 30 [3] or 56 µs [5]), corresponds to the penetration of the projectile within the fragmented – partially or fully damaged – ceramic for which the size and the mobility of fragments play a key role on the resistance of the ceramic [10]. Thanks to X-ray radiography analysis, it was observed that the ceramic (for a boron carbide (B_4C)) is actually stopped 56 µs after impact [5]. During the penetration of a ceramic armour system by an AP projectile, less than 1% of the total impact energy is estimated to be absorbed by the fracturing of the ceramic [12], and so debris ejecta do participate to a large proportion of removal of the total energy. It appears that the contribution of fragments resistance in the penetration stage plays a major role, although the ceramic has already been strongly cracked upon impact. Thus, the penetration resistance of the fragmented media needs to be considered as well as the material parameters of the ceramic prior fragmentation (such as Hugoniot Elastic Limit (HEL), tensile strength, *etc.*) to design improved shielding.

The resistance of a fragmented ceramic under impact loading was investigated in the 2010s in the PhD works of Rossiquet [13] and Zinszner [10] with a new "tandem configuration" developed by Zinszner, Forquin and Rossiquet [14,15]. In this test, the ceramic is fragmented upon normal impact of a flat-end projectile, as a first step. *Post-mortem* observations of the fragmented SiC ceramic are conducted to analyse the cracks density λ_{cracks} (example in Figure 1 (a)) as studied by Zinszner, Forquin and Rossiquet [15] and Forquin *et al.* [16]. Circles of given radius r were drawn from the impact point and the number of cracks N_{cracks} crossing each circle was counted. This number was divided by the arc length ($L_{arc} = r.\theta$ where the radius r is the distance from the impact point and θ the arc angle in radian), all of which being raised at the power of three. Indeed, the fragmentation process is a 3D process and cracks are supposed to be triggered from volume defects (*i.e.* defects randomly distributed in the volume). In Forquin and Andò [17], the fragments distribution of a target subjected to an Edge-On-Impact (EOI) test was investigated by means

of X-ray micro-computed tomography, Figure 1 (b). Following the normal impact, a perforating (or rather penetrating) impact of a penetrating projectile is conducted as a second step, in order to evaluate the resistance of the pre-fragmented ceramic. The velocity profile measured on the rear face of the backing is compared to the data of numerical simulation with the aim to identify Drucker-Prager (DP) plasticity model [18], which provides a describing of the dynamic behaviour of the fragmented ceramic. The DP model was formerly considered to numerically model the mechanical response of a fragmented ceramic in the modified Wilkins' model [19]. This latter model [20,21] also includes a tensile damage model to simulate the growth of fracture conoid (Hertzian cracks) [20,21]. DP is a pressure-dependant model defined in 1952, usually applied to granular medias which exhibit a small or nil cohesion strength. Anderson Jr., Chocron and Behner [22] postulated that the DP constitutive model could represent the penetration response of a SiC, pre-damaged by thermal shock and load-unload cycles. The three model parameters of the DP model were determined by inverse approach and a good correlation with experimental results was obtained with several sets of parameters. However, it was pointed out by Anderson Jr. *et al.* [23] that a projectile necessarily penetrates a damaged fragmented media whatever the penetration velocity as the damage front propagates faster than the front of the impacting rod. More recently, an identification of the DP model parameters was performed by Zinszner [10] based on the numerical simulation of the penetration impact of a conical end projectile (in tandem configuration) through a pre-fragmented SiC ceramic. The numerical velocity profile matches with experimental results, which validates the numerical model, Figure 1 (c). The development of ceramic materials aiming to mitigate cracks propagation under impact loading is something that attracted global attention in ballistics. Since 2003, Forquin *et al.* [24] have investigated the use of a SiC ceramic infiltrated with an aluminium alloy for reducing the mobility of fragments and increasing the resistance towards a second impact. It is the reason

why, ceramics having high fracture-toughness could be good candidates as front plate of bilayered configurations.

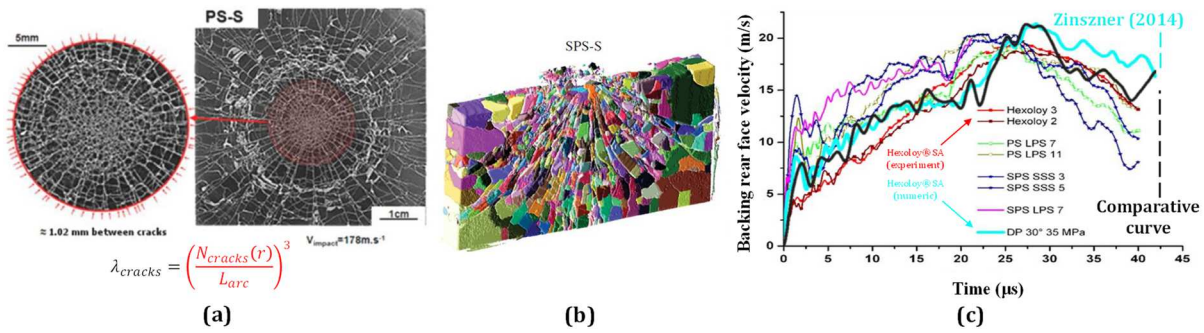

Figure 1. Estimation of the density of cracks in a fragmented SiC ceramic subjected to normal impact (adapted from: [15]). (b) 3D X-ray and *post*-treated rendering of a fragmented SiC grade after EOI [17]. (c) Numerical simulation of a penetrating impact test according to [10] curve and as obtained in this work (curve in black colour), compared to the experimental velocity profile (adapted from [10]). [2-column fitting]

Biological materials (such as: mollusc shells and seashells, arthropod exoskeleton, antlers, tusks and teeth, bird beaks, bones, coral, … [25]) adopt microstructures that have drawn attention to researchers because they exhibit exceptional mechanical properties *i.e.* high stiffness, high strength and high toughness, while keeping a moderate density [25]. Their components are organised in complex hierarchical structures although they are made of basic natural polymers and minerals that are relatively weak when taken individually [25]. The reason of their superior performances exceeding what can be achieved using the same synthetic materials comes indeed from the complex microstructure they adopt (organic/inorganic laminar structures, presence of porous and fibrous elements) and the interaction between each constituent [25]. A material which brought attention to researchers working in materials science is the nacre that covers the surface layer of many seashell species (*e.g.* abalone Mollusca): it is a platelet-reinforced composite made of calcium carbonate $CaCO_3$ (calcite or aragonite minerals [26]) with an organic matrix made of α-amino acids (containing aspartic acid, cysteine, glycine, alanine [26]) and polysaccharide [27]. As noted by Chen *et al.* [25], nacre, like other biological materials, adopts an increasing

complexity of its hierarchical structure as the dimension becomes smaller. The nacreous architecture is built with "bricks" of stacked platelets (~ 500 nm thick in abalone [25]) glued at their interfaces with an organic "mortar" matrix (20–50 nm thick in abalone [25]), hence the so-called "brick and mortar" (BM) microstructure name. In addition, inter-tile mineral bridges within the "mortar" help to stick the platelets together as well as providing toughness resistance [25]. This anisotropic, or rather orthotropic [28], type of material is in majority composed of $CaCO_3$ ceramic (95 wt.% inorganic, 5 wt.% organic in abalone [25]) and can exhibit a fracture energy 3000 times higher than the ceramic alone [27]. Damage-resistance is achieved through different failure mechanisms depending on the loading direction. Menig *et al.* [29] characterised abalone shells under quasi-static and dynamic loadings, and Chen *et al.* [25] described the influence of the abalone shell microstructure in a review, dedicated to mechanisms. When loaded perpendicularly to the platelets, failure modes correspond to axial splitting in compression (compressive strength $\sigma_c = 540\ MPa$), bridging fracture and extension of the organic layer in tension (ultimate tensile strength $\sigma_t = 5\ MPa$). When loaded in parallel to the platelets, failure modes consist in axial splitting mode and plastic microbuckling (kinking) in compression ($\sigma_c = 235\ MPa$) and tiles sliding with brittle inter-shear failure in tension ($\sigma_t = 170\ MPa$) [25,29]. The dynamic compression strength of abalone BM microstructure was found to be 50% higher than its quasi-static strength [29]. The organic layer plays a significant role in controlling damage since it gives viscoplastic deformation as well as crack deflection [61]. Radi *et al.* [30] developed a series of mesoscopic numerical simulations of nacre using Discrete Element Method (DEM) and concluded that the ratio of interface strength to tablet drives the regime of failure. Increasing the interface strength compared to the matrix strength (ratio tending to 1) should lead to a brittle and catastrophic failure and should be avoided. More details upon the role of the polymer (or even metallic [31]) phase can be found in other works ([32–35]). Several processing strategies were

attempted to replicate the layering of nacre. Bouville *et al.* [36] engineered a BM artificial nacre entirely mineral, of composition 98.5 vol.% Al_2O_3, 1.3 vol.% SiO_2 and 0.2 vol.% CaO. This synthetic nacre is not a ceramic/polymer composite but a ceramic/ceramic one, mostly composed of alumina since both the platelets and the matrix are made of alumina material. In fact, the presence of a polymeric phase brings toughness but decreases strength [37] and high-temperature capabilities [36]. Freeze-casting and-drying processes were used on the green body during the preparation, known as ice-templating. The latter technique is a directional freezing under a flow method of the suspension allowing obtaining long-range order of parallel ice crystals. The growth of ice crystals acts as a driving force for the local self-assembly of the anisotropic platelets. These crystals of ice are then removed by vacuum freeze-drying. Supplementary details on such process can be found in [38,39] and more details are available in the patent WO 2015/189659 "Ceramic product with oriented particles and method for the production thereof" [40]. The sintering (of the 86%-porous sample) is realised by Spark Plasma Sintering (SPS) at 1500 °C with pressure assistance (100 MPa). The nacre-like alumina in Bouville *et al.* [36] was tested in 3-point bending tests to point the importance of the synergetic effects of the nacre constituents (platelets + glass phase + bridging nanoparticles). This material was compared to a first "partially"-like nacre without nanoparticles (platelets + glass phase) which exhibits a classical brittle response even if a high fracture-toughness is achieved compared to a conventional alumina ceramic (6.1 $MPa.m^{1/2}$ vs. 3.5 $MPa.m^{1/2}$). This nacre-like alumina was also compared to a second "partially"-like nacre, without glass phase (platelets + nanoparticles), which exhibits a significant toughening stage with high failure strain, but with a lower flexural strength σ_w (~ 275 MPa, against ~ 325 MPa for a reference alumina, ~ 350 MPa for the material without nanoparticles but with platelets + nanoparticles and ~ 450 MPa for the nacre from Bouville *et al.* [36]). The latter authors distinguish the "intrinsic" and "extrinsic" toughening phenomena. Intrinsic phenomena

include the inherent strengths of the matrix, of the platelets and of the bridges, the visco-plasticity of the matrix and the crack deflection at the platelet interface. Extrinsic phenomena ("no true ductility") that results in stable crack growth, are explained by the contribution of each nacre constituent, including visco-elastic deformation of the matrix, bridge rupture, and inelastic shearing and frictional sliding during platelet pull-out. At the crack tip, crack branching, crack bridging, multiple cracking and platelet delamination release the locally high stresses. Numerical model of a BM armour consisting of B_4C tablets and polyurea tablet/tablet interfaces was investigated in [41]. Another numerical model using layer waviness and cohesive interface in an aluminium alloy 7075 inspired by nacre was developed in [42]. Both studies concluded that better ballistic performances were achieved compared to their monolithic counterpart, but no experimental data that permits to confirm or infirm these results. To the best of authors knowledge, no fragmentation testing technique has ever been applied to nacre, to the exception of EOI tests applied to nanolayered Ti_3SiC_2 (MAX phase) [43].

The two materials considered in the present study named 98% Al_2O_3 and MAINa (which means Nacre-Inspired Alumina Material or *Matériau Aluminé Inspiré de la Nacre* in French) are presented in the second section, while tandem tests are presented in the third section. Normal impact test results are presented in the fourth section. Next, the penetrating impact is numerically simulated in the fifth section in order to identify the Drucker-Prager parameters by means of a numerical inverse approach, thus simulating the fully damaged material. Finally, the microstructure influence of both alumina ceramics on their fractured (damaged) strength is discussed.

2 Ceramic samples

2.1 Microstructures

2.1.1 Alumina (Al_2O_3) ceramic

The reference ceramic (Figure 2, left) is a dense alumina, 98% pure in mass, that is produced with a classical route. The production of the ceramic starts with the selection of the raw powder that strongly influence the performances of the material [13]. The green-body (mixture of ceramic with organic and inorganic additives before sintering) is shaped by uniaxial-pressing. The sintering step consists in consolidating the material by heat action without (solid-state) or with partial (liquid-state) melting of one or several constituents in a kiln. During this step, grains merge at their boundaries (coalescence) and the porosity content is considerably reduced (densification, dimensional shrinkage) [44,45]. The sintering is performed pressure-less (PS), that constitutes a traditional and economical technique to sinter large quantities of ceramic products [13].

2.1.2 Nacre-like alumina (MAINa) ceramic

The MAINa is described in the patent "Dense sintered product" (WO 2018/141736) [46]. The platelets (Ronaflair® White Sapphire powder from Merck group) are the first particulate fraction (or platelet fraction) of approximate size 5–10 µm with 500–1000 nm in thickness. The second particulate fraction (size < 1 µm) is made of three constituents. First, mineral ceramic bonds form bridges between the platelets that correspond to nanoparticles of YSZ (Yttria (Y_2O_3)-partially Stabilised Zirconia (ZrO_2)) from TZ-3Y-E® (3 mol.% Y_2O_3) powder and of approximate average size 40 nm [47] according to the supplier (from Tosoh). Second and third, additional smaller nanoparticles (~ 20 nm) of silica (SiO_2) and calcia (CaO) of liquid-phase precursors are present as glass or glass-ceramic particles to foster filling the remaining gaps during the sintering stage. Some of these nanoparticles deposit on the surface of platelets and form nano-asperities responsible of part of the energy dissipation by frictional

218 sliding during platelet pull-out and breaking of the bridges. In terms of composition, the
219 material is made of 94.7 wt.% Al_2O_3, 4 wt.% ZrO_2, 0.75 wt.% SiO_2, 0.25 wt.% CaO and 0.3
220 wt.% of other elements (of which less than 0.1 wt.% of MgO). The processing strategy and
221 the manufacturing processes can be divided into the three following steps.

222 Powder preparation of an aqueous colloid: An anionic dispersant (Darvan® 7NS from
223 Vanderbilt Minerals, sodium methyl methacrylate (Na-MMa)) and additives are mixed
224 together in de-ionised water with a suspension of nanometre powders (ZrO_2, SiO_2, $CaCO_3$),
225 then agitated (ball-milled with Al_2O_3 balls) overnight (at least 12 hours) to ensure a proper
226 deagglomeration. Al_2O_3 platelets are then added 3 hours before the end of the cycle (to avoid
227 any excessive breakage by the milling media) with a thickener (Carbopol® EDT 2691 from
228 Lubrizol Corporation).

229 Freezing of the green body: The obtained green body is poured in a stainless steel
230 before the recipient be plunged in liquid nitrogen for rapid freezing (around 20 minutes). Ice
231 crystals are created. The frozen green body is frozen-dried for about 5 days. The intermediary
232 product, a dried bloc with low mechanical properties, is ground with a hand press before
233 being sieved at 1 mm to eliminate the biggest agglomerates.

234 Thermal treatment then pressure-assisted and Field-Assisted Sintering Technique
235 (FAST): The ground powder is thermally treated at 450 °C for 1 hour (50 °C/h of temperature
236 ramp) and fired until 900 °C (100 °C/h) then cooled (-300 °C/h), so that the organic
237 constituents are removed (debinding) and the nanoparticles pre-sinter on the platelets. The
238 nanoparticles of the glass phase sinter at lower temperatures than platelets due to their higher
239 surface area and curvature. The ZrO_2 nanoparticles are not completely dissolved in the glass
240 phase thanks to short processing times during the densification. The precursor particles (SiO_2
241 and CaO) may delay the densification of the ZrO_2 nanoparticles by preventing their contacts
242 with the platelets. Following this, the powder is placed in a cylindrical graphite matrix to be

pressed at 5 MPa. Afterwards, the die is placed within a kiln and sintered via pressure-assisted FAST (or pressure-assisted SPS technique) at around 1500 °C (100 °C/min) with 50 MPa. Compared to conventional sintering, SPS technique produces a more homogeneous heating, higher heating rate, finer grains and higher relative densities. The elevation of temperature is due to the Joule effect of a graphite die travelled by a Direct Current (DC). After sintering, the platelets are aligned to each other.

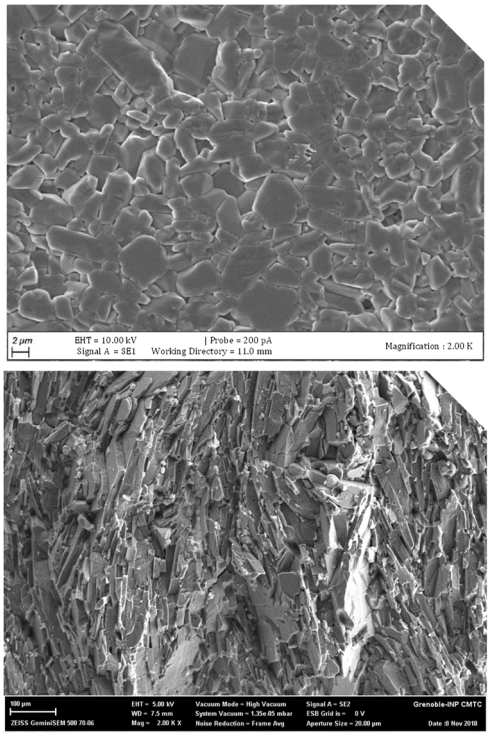

Figure 2. SEM micrographs of Al_2O_3 (courtesy of Saint-Gobain, at the top) and MAINa fracture surface (3SR, at the bottom) showing its BM microstructure. [single-column fitting]

2.2 Materials properties

Some physical properties of both materials are reported in Table 1. The densities ρ come from material data sheets to be compared to the theoretical densities ρ_{th} of 3890 kg.m^{-3} for Al_2O_3 and 3933 kg.m^{-3} for MAINa. The porosity p of Al_2O_3 is deduced from its purity, the MAINa's is estimated by comparing its theoretical density (~ 4032 kg.m^{-3}) and the measured Archimede's density (~ 3933 kg.m^{-3}). The grain size (for Al_2O_3) and the platelet size (for MAINa) are provided by Saint-Gobain thanks to SEM images.

Grade	ρ (kg.m^{-3})	p (%)	Grain (Al_2O_3) / Platelet (MAINa) size (µm)
Al_2O_3	3900	~ 2	~ 2.6
MAINa	3930	~ 3	~ 5 – 10 (diameter) ~ 0.5 – 1 (thickness)

Table 1. Physical properties of the two Al_2O_3 grades (Saint-Gobain data).

Some basic mechanical properties are reported in Table 2. Relative to MAINa, which is an anisotropic material, data of the latter refer to its characterisation when platelets are oriented in a perpendicular way to the direction of loading. The hardness H_V was measured by Vickers indentation by using a Buehler 6030 micro-durometer with a diamond squared-base pyramid in accordance with the NF and EN 843-4 standard [48]. The samples were beforehand embedded in a resin then polished. The hardness of Al_2O_3 was tested with a 0.2-kg load ($H_{V_{0.2}}(Al_2O_3) = 1735$) and the nacre's with a 0.1-kg load ($H_{V_{0.1}}(nacre) = 1600$). Hardness data are expressed in Pascal unit of pressure (GPa) later on in Table 2. The Young's modulus E of Al_2O_3 was calculated using a resonance measurement method in accordance with the ASTM C1259 standard [49]. Subject to a mechanical impulsion, the mechanical vibration is detected and converted into an electric signal, which is analysed to isolate fundamental frequency. Using flexural specimens, the flexural vibration mode provides the elastic modulus. Using rectangular specimens, both the flexural and the torsional vibration modes provide both the Young's and the shear moduli. The two Young's moduli obtained with both types of specimen are almost identical. The value delivered by the rectangular specimen reported in Table 1 will be kept as this geometry also delivers the shear modulus. The Young's modulus E of MAINa was calculated using bending test results (Table 1). Considering the Young's modulus and the shear modulus (obtained from the resonance frequency in torsional vibration mode), the Poisson's ratio ν can be deduced according to ASTM C1259 [49]. The Modulus Of Rupture (MOR) is measured by 3-point bending (or

flexural) tests performed with ~ 45×4×3 mm^3 (rectangular cross section) polished and chamfered test beams, in accordance with the NF EN 843-1 standard [50]. Tests were conducted with a 10-kN Shimadzu loading press. Thanks to the MOR value, the mean failure stress σ_w is calculated with a Weibull's analysis [51,52]. The stress data displayed in Table 2 are given as function of an effective volume V_{eff} (1 mm^3) based on equation (1) [53].

$$V_{eff} = \int_{\Omega} \left(\frac{\langle \sigma(\underline{x}) \rangle}{\sigma_{max}} \right)^m . d\omega, \quad \textbf{(1)}$$

where m is the Weibull's modulus, $\sigma(\underline{x})$ is the longitudinal stress in the tested sample at a point of coordinates, σ_{max} is the maximum principal stress, and $\langle . \rangle$ are the Macaulay brackets that take the positive (tensile) value of stress. In 3-point bending, the equation (1) becomes (2):

$$V_{eff} = \frac{V}{2.(m+1)^2} \quad \textbf{(2)}$$

Given the Weibull's modulus m, the mean strength $\sigma_{w,ref}$ associated to a reference effective volume ($V_{eff,ref}$ = 1 mm^3) can be calculated in (3):

$$\sigma_{w,ref} = \sigma_{w,bending} . \left(\frac{V_{eff,bending}}{V_{eff,ref}} \right)^{\frac{1}{m}} \quad \textbf{(3)}$$

where: $\sigma_{w,bending}$ is the mean tensile strength (also called Modulus Of Rupture or MOR) equal to 367 MPa ($V_{eff,bending} \sim 3.0\, mm^3$) and 581 MPa ($V_{eff,bending} \sim 1.2\, mm^3$) for Al_2O_3 and MAINa, respectively. The larger number of specimens tested in bending (≥ 20) enables to deduce the Weibull's modulus [51,52] of Al_2O_3 (Table 2). As regards MAINa, the Weibull's modulus reported in Table 2 originates from the nacre-like alumina material. Finally, the fracture-toughness K_{I_c} of the two ceramics was determined in accordance with the ASTM C1421 standard [54] using the SENB (Single-Edge Notched-Beam) method, which consists in a 4-point bending test performed on a pre-notched sample. The notch was

machined with a diamond saw and was ended with pre-crack of around 0.3 mm in length with a razor blade coated with a diamond paste to create a stress concentration at the notch tip. In MAINa, K_{I_c} was equal to 6.15 ± 0.26 MPa.m$^{1/2}$. The interest of the BM microstructure is that the "apparent" fracture-toughness increases as crack propagates due to energy dissipation. This enhanced toughening resistance is known as R-curve effect and is characterised by the apparent fracture-toughness parameter K_J in MPa.m$^{1/2}$. The measured K_J was 9.84 ± 0.34 MPa.m$^{1/2}$. It can be noted that compared to Al_2O_3, K_{I_c} is 26.54% higher and K_J is even 102.5% higher.

Grade	H_v **(GPa)**	E **(GPa)**	ν **(-)**	m **(-)**	σ_w **(MPa)**	K_{I_c} **(MPa.m$^{1/2}$)**
Al_2O_3	17.0	369	0.20	8	421**	4.86 (± 0.50)
MAINa	15.7	344	0.26	14*	589**	6.15 (± 0.26)

** Another nacre-like alumina material / ** For $V_{eff,ref}$ = 1 mm^3*

Table 2. Mechanical properties of the two Al_2O_3 grades (Saint-Gobain data).

3 Tandem test: normal and penetrating impact test

3.1 Introduction to tandem test

The tandem test represented in Figure 3 (a) is a two-step experimental testing technique. It was developed in previous research works [13,10,15] to evaluate the behaviour of a fragmented ceramic under impact. The first test, called "normal impact test", is conducted with a flat-end projectile (Figure 3 (b)) and uses a confining system to prevent any loss of fragments after impact. The second test, called "penetrating impact test", aims to analyse the residual penetration resistance of the fragmented ceramic. It consists in impacting the damaged target with a conical end or hemispheric end projectile as shown in Figure 3 (b). The mechanical behaviour of the fragmented ceramic is deduced from particle velocity measurement on the rear face of the backing.

The dimensions (length (L) × width (W) × thickness (t)) of the ceramic plates are 50 × 50 × 7 mm^3. Finish required rectification to ensure a strict parallelism of the surfaces (0.05 mm max. gap); no polishing was required. The exact dimensions and densities of the ceramic plates, the impact velocities V_{impact} and the projectile mass m are reported in Table 3. Projectile impact speed is set to 175 m/s in case of normal impact and penetrating impact with a conical-head projectile, whereas an impact speed of 145 m/s is set in the case of penetrating impact conducted with a hemispherical-head projectile. Tests "1" and "1b" correspond to distinct targets subjected to tandem tests. Tests "2" refer to targets subjected to normal impact and X-ray tomographic evaluations. The projectiles are made of steel. The three projectile geometries own the same approximate mass (9.10 g) and are placed inside a Teflon® sabot having a diameter adjusted with the inner diameter of the gas launcher tube (~ 20.10 mm). No visible deformation of the projectile in any test was observed after both stages of impact.

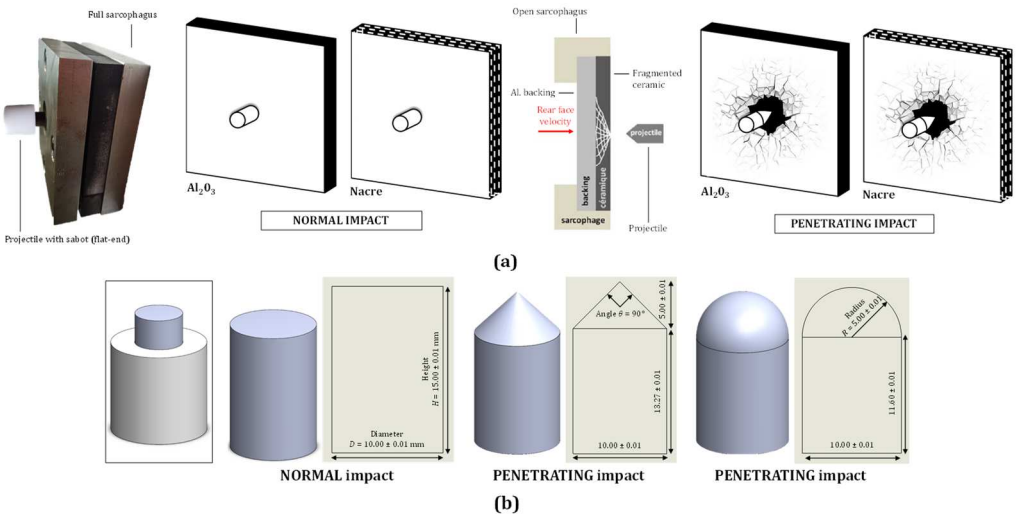

Figure 3. (a) Tandem test (normal impact view, penetrating impact sketch (adapted from: [10])) with orientations of interest. (b) Projectile shapes and dimensions. [1.5-column fitting]

Sample name	**Dimensions (mm)**	ρ_{exp} **(kg.m^{-3})**	**Impact test**	V_{impact} **(m/s)**	**Projectile** m **(g)**
Tandem-Al$_2$O$_3$-1	50.41 × 50.30 × 7.03	3896	Normal	175.05	9.11
			Penetrating	175.05	9.13

Tandem-Al_2O_3-1b	50.65 × 50.49 × 7.14	3805	Normal	188.20	9.09
			Penetrating	184.21	9.16
Normal-Al_2O_3-2	50.50 × 50.32 × 7.17	3814	Normal	181.39	8.95
Tandem-MAINa-1	50.20 × 50.30 × 6.27	3926	Normal	184.21	9.10
			Penetrating	178.16	9.11
Tandem-MAINa-1b	50.18 × 50.15 × 6.30	3861	Normal	172.31	9.10
			Penetrating	178.46	9.14
Tandem-MAINa-1b Hemi	50.11 × 50.01 × 6.28	3935	Normal	172.32	9.11
			Penetrating	142.39	9.07
Normal-MAINa-2	49.62 × 49.44 × 5.63	3902	Normal	181.70	9.02

Table 3. Dimensions and experimental densities (ρ_{exp}) of the ceramic samples, type of impact (normal or penetrating), velocities and mass of the projectiles.

3.2 Normal impact test

In the first stage, a normal impact is performed against an aluminium-ceramic-steel sandwich configuration. The numerical design and optimisation of this configuration was studied in [14]. The different pieces of the sarcophagus device are visible in the Figure 4 (a). An aluminium alloy plate of same size (49.40 × 49.40 mm^2) but of smaller thickness (6 mm) is used as backing (properties in Table 4). Steel wedges of few mm^2 (*cf.* Figure 4 (b)) are glued on the rear face corners of the ceramic to impose a 0.1-mm gap, which ensures an impedance discontinuity that promotes the fragmentation process in the ceramic. At the top of the ceramic, a thin (1 mm thick) steel plate (49.40 × 49.40 mm^2) is placed to prevent any fragments ejection. The ceramic sandwiched between the aluminium backing and the steel front sheet is placed in a sarcophagus configuration. The assembly steps are visible in the Figure 4 (b).

3.3 Penetrating impact test

The second stage of tandem test consists in impacting the fragmented ceramic backed with the same aluminium plate as in normal impact test but using a hemispherical or conical end projectile. A stop-sabot device is placed to prevent the impact of the sabot against the target during the recording time. The sarcophagus front plate and the thin steel plate are removed prior the second impact.

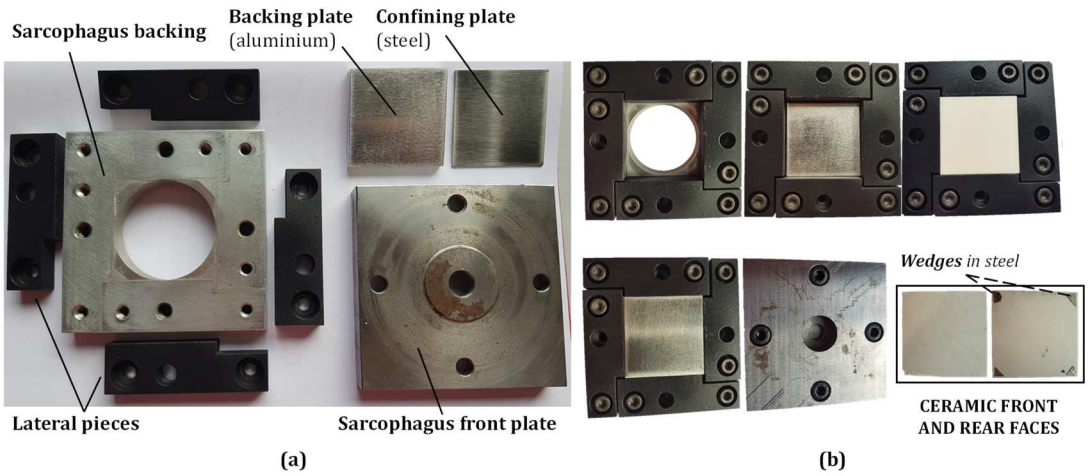

Figure 4. (a) Exploded view of the tandem sarcophagus with (b) successive assembly steps of the tandem sarcophagus: screw of the aluminium lateral pieces, positioning of the aluminium backing, positioning of the ceramic plate (with wedges), positioning of the steel front plate and closing of the assembly. [2-column fitting]

Grade	ρ (kg.m^{-3})	E (GPa)	ν (-)	R_e (GPa)
Aluminium 7075	2800	72	0.33	0.45
High-strength steel	7785	210	0.30	1.35

Table 4. Physical and mechanical properties of the aluminium alloy and of the steel alloy (applies for the steel projectiles too).

The front face of the target is visualised with an ultra-high-speed camera (Kirana®, 5 Mfps capacity, 924×768 px, 180 images), set to 500 kfps with 2 µs exposure time, except for "Tandem-Al_2O_3-1" and "Tandem-MAINa-1" recorded using 200 kfps. The triggering is made with a laser interferometer (1.5 MHz of bandwith, maximum measured velocity 20 m/s) pointed toward the rear surface of the aluminium backing plate. The measured velocity cannot

exceed 23 m/s due to the limited range of measured velocity with this equipment. In addition, two high-power flash lights are placed close to the zone of visualisation to deliver enough light during recording. The triggering of the flash is performed when the projectile crosses one of the three velocity barriers that are used to determinate the impact velocity.

3.4 Fractography after penetrating impact tests

Next to penetrating impact, fragments of ceramics were analysed through SEM using secondary electrons to investigate the topology information of the fracture surface. The detector is placed in a grazing position.

The fracture surfaces for Al_2O_3 exhibits an intergranular-dominated fracturing mode (as observed in Chen *et al.* (2006) [55] on alumina subjected to plate-impact below the HEL), although some transgranular modes are also visible (cleavage, river patterns, feather markings). Images of MAINa fragments put into evidence additional mechanisms of energy dissipation, such as frictional sliding during platelet pull-out, delamination of platelets and crack deflection at the platelet interfaces.

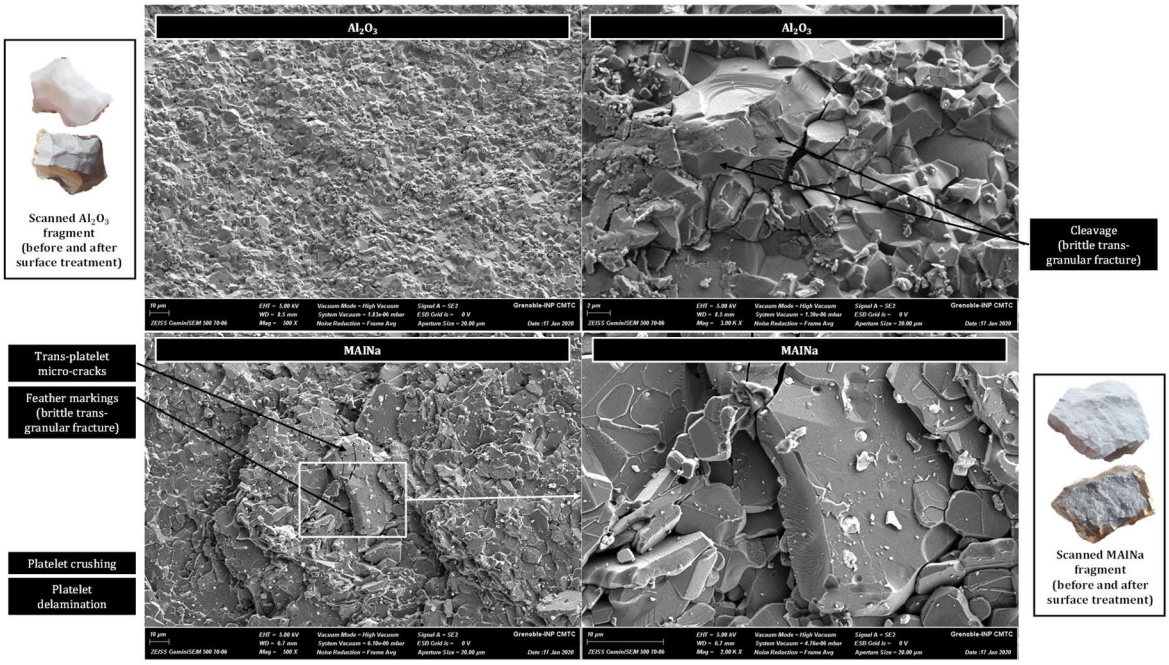

Figure 5. SEM micrography on recovered fragments from Tandem-Al_2O_3-1b and Tandem-MAINa-1b (1 to 1.5 mm approximate size along the major axis) on which silver lacquer and graphite were deposited to allow for conductivity and evacuating electric charges. [2-column fitting]

4. Fragmentation under normal impact experiment

4.1 Visualisation of cracking pattern

When the sarcophagus front plate and the thin steel sheet are taken off, the fragmentation pattern for each sample is revealed (Figure 6). The failure pattern of the samples with the same microstructure shows a good repeatability. Such "deterministic multiple-fragmentation feature" was already noted in previous works (the reader is referred to [16]). Since the samples are not polished, it is difficult to count the cracks by direct visual observation, especially for Al_2O_3 for which crack opening seems to be smaller than MAINa (the lower the toughness, the lower the crack opening). Concentric radial circles of cracks are found in abundance.

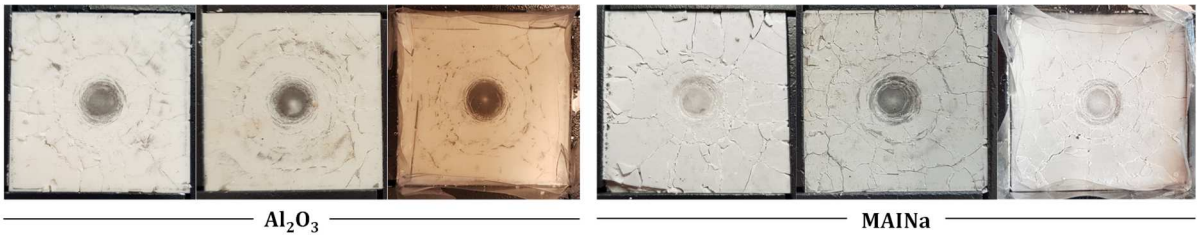

Figure 6. *Post-mortem* observations after normal impact of Al_2O_3 and MAINa (from left to right: Tandem-Al_2O_3-1, Tandem-Al_2O_3-1b, Normal-Al_2O_3-2, Tandem-MAINa-1, Tandem-MAINa-1b and Normal-MAINa-2).

[2-column fitting]

4.2 Evaluation of cracking density

The samples named Normal-Al_2O_3-2 and Normal-MAINa-2 were analysed through tomography scanning. Prior to impact, a plastic sheet was put to encompass the ceramic and the steel plate so that the ceramic target can be vacuum infiltrated (equipment: VACUMET 52® from Mekton Instruments Inc.) with a hyper-fluid resin after impact. After normal impact, the impacted steel plate was removed before infiltration of the fragmented ceramic with vacuum set down to 600 – 650 mmHg (0.80 – 0.87 bar). The infiltrated sample is then cured for 24 hours. Next, 3D field X-ray micro-tomography is performed within the tomographic platform in 3SR. An X-ray beam is generated with a 100-kV voltage and a 250-µA current (tube power of 25 W). The duration of scanning is 112 min producing a set of 1800 slices (400 pixels through the thickness, 1800 pixels through the length and width) with 30-µm of voxel size. The source consists in an electron beam accelerated against a tungsten (W) target. An aluminium filter (0.5 mm thick) is placed in front of the source in order to pre-harden the signal by attenuating low-energy photons. Ring artefacts, caused by shifts of the sample on the rotation axis after reconstruction, are decreased thanks to a ring filter. Three different slices from Computed Tomography (CT) are shown in Figure 7.

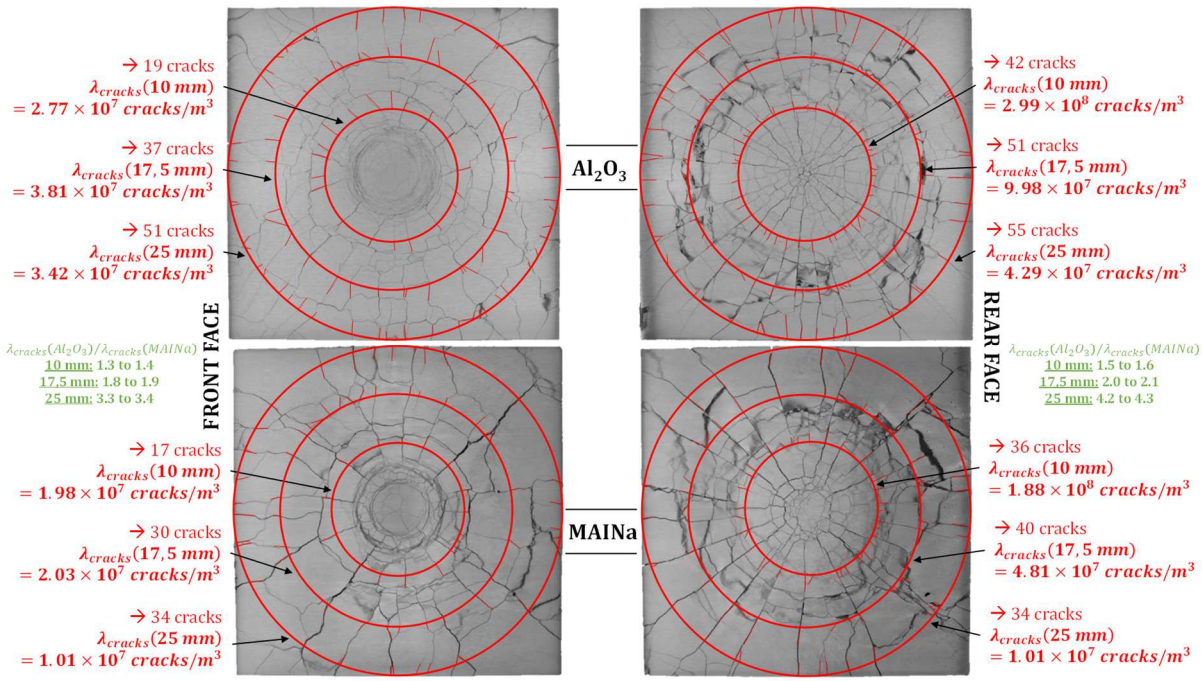

Figure 7. *Post-mortem* evaluation of cracks density based on tomographic images. [2-column fitting]

When looking at the Figure 7, MAINa clearly exhibits fewer cracks than the Al_2O_3 target, so possibly larger fragments. On the front and rear faces from the tomographic images, different circles centred on the impact point were defined considering radius of 10, 17.5 and 25 mm, which correspond to different levels of strain-rates (*cf.* next sub-section). The cracks density λ_{cracks} is calculated and marked down. It appears to be about 2 to 3 times smaller in MAINa sample than in Al_2O_3 on both front and rear faces. Thus, larger fragments are expected in MAINa than in the Al_2O_3 ceramic sample. More specifically, fragments in MAINa that are far from the impact seem to be drastically larger. For instance, on the front face, the ratio of the cracks density measured in MAINa to the one of Al_2O_3 is equal to 1.3 to 1.4 at 10 mm from the impact point, while it increases to 3.3 to 3.4 at 25 mm.

4.3 Estimation of the stress-rate in the ceramic plate

The normal impact, that is the first stage of tandem test, is simulated with the ABAQUS Explicit Finite Element (FE) software. The impact velocity with the flat end impactor is set to 175 m/s. Two symmetry planes are considered. The mesh is made of ~ 0.5-

mm C3D8R elements (3D 8-node linear brick, reduced integration, hourglass control). The material parameters considered for the steel projectile and the steel confining plate on the top of the ceramic are reported in the Table 4. An elasto-plastic model with an elastic limit R_e is considered for the projectile and the confining plate whereas the behaviour of the ceramic is modelled with the elastic parameters provided in Table 2. Surface-to-surface contact algorithm applies with a friction coefficient of 0.2.

In the wake of the compressive wave, fragmentation process develops on the rear face due to tensile hoop stresses induced by the radial motion of the matter. The evolution of hoop stresses $\sigma_{\theta\theta}$ as function of time is plotted considering different radii defining a cylindrical coordinate system with the opposite face of the point of impact as origin, Figure 8. The stress-rate $\dot{\sigma}$ then is deduced considering the slope between 200 MPa and 400 MPa, 400 MPa corresponding approximately to the tensile strength of alumina measured in 3-point bending. The change of hoop stress-rate with the radius is plotted as function of the radius in the Figure 9. It is observed that the hoop stress-rate rapidly decreases with the radius until 12.5 mm and is fluctuating in between 300 and 600 MPa/µs beyond 12.5 mm. Accordingly, the stress-rate at r = 10 mm ($\dot{\sigma}$ = 850 MPa/µs) is much higher than the stress-rate at r = 17.5 mm ($\dot{\sigma}$ = 312 MPa/µs), which explains the higher cracking density noted at r = 10 mm compared to r = 17.5 mm, as observed in the previous 4.2 section.

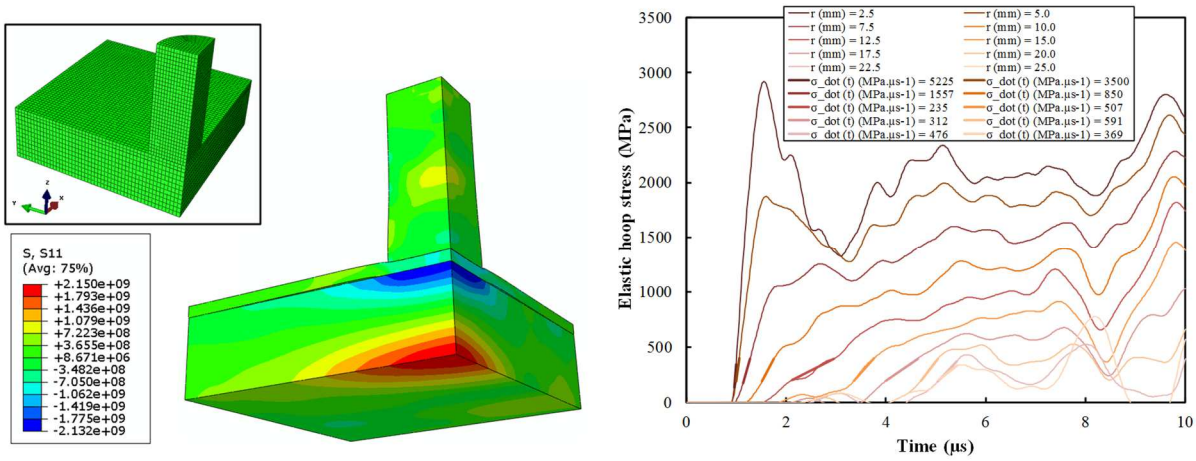

(a) (b)

Figure 8. Numerical simulation of normal impact considering an Al_2O_3 target impacted at 175 m/s. (a) S11 stress field at 5 µs after impact. (b) Profile of hoop stresses on the rear face of the ceramic as function of time. [1.5-column fitting]

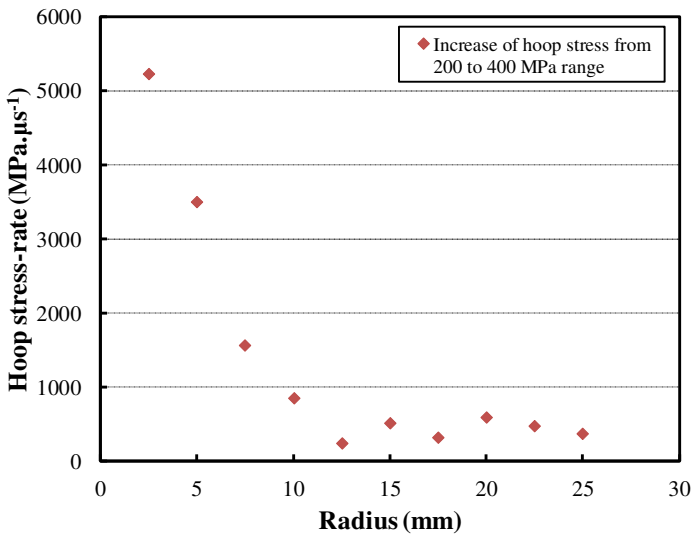

Figure 9. Change of the hoop stress-rate with the radius in the rear face of the Al_2O_3 ceramic. [single-column fitting]

4.4 Evaluation of fragments size by tomography

In this part, the fragments distribution is analysed. The tomographic greyscale images are rescaled in Fiji (an open-source software program for image analysis) using a bilinear interpolation to reduce the size and so the processing time of the multi-image, passing from 1800 × 1800 × 400 px^3 to 900 × 900 × 200 px^3. Then, the images are loaded in a Python

environment to be treated with the imported SPAM [56] package. The processing steps applied to the greyscale images as already used in Forquin and Andò [17] are the following: first, a 3D Sobel operator is employed for the detection of cracks. Next, a 3D median filter (reduces noise), a thresholding ("black-and-white" two-value binarised image), a 3D marker-based watershed algorithm on the Euclidean distance (segmentation of fragments) followed by a labelling (assigning a value for each separated fragments), and a manual label merging to join non-physically separated fragments and compensate over-segmentation, are applied. The same *post*-treatment methodology as in [17] was considered in the present work with the following change: a hessian filter is rather applied first and foremost to allow a proper separation of the different fragments. As shown in Figure 10, the maximum hessian filter better discriminates all the cracks.

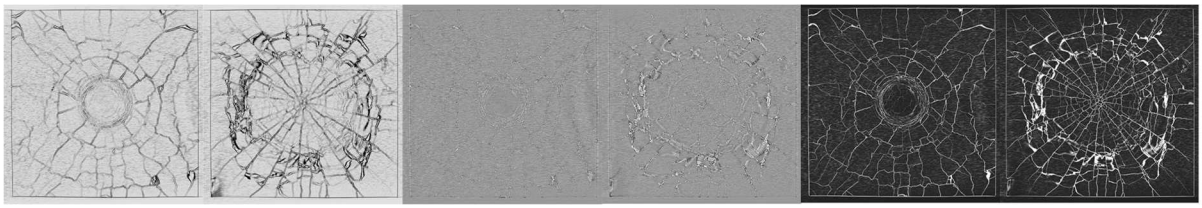

Minimum eigenvalues ***Intermediate eigenvalues*** ***Maximum eigenvalues***

Figure 10. Hessian-filtered images of Al_2O_3 for different eigenvalues components. [2-column fitting]

Then, the filtered images are binarised with threshold parameter, but the resulting image being noisy, a function is used to detect the smallest labels (considered as noise) in order to delete them. Finally, SPAM owns a label toolkit to rapidly create labelled images thanks to a watershed for separating the single interconnected solid phase into individual particles [49]. However, in the watershed process, the glue gets also labelled into different fragments, so a manual operation is required to delete them. To give an idea to the reader, after 7 (9 for MAINa) manual iterative operations including at maximum 5 to 10 labels, all the glue was managed to be removed. The different steps are reported in Figure 11. The fragments are coloured at the end with a colour panel ("glasbey inverted") plugin. While the code seems to be satisfactory for Al_2O_3, a visual inspection in Figure 12 shows slight over-

segmentation of the largest fragments in MAINa, as pointed out by red arrows on some fragments. This issue was already encountered by Forquin and Andò [17]. To counter-act this, an additional step is added that consists in a manual step of label merging that can be automatized with a SPAM function named "label.contacts.detectAndFixOversegmentation(lab, nVoxThreshold)" (with *lab* the multi-array matrix image after the "g" step and *nVoxThreshold* the number of voxel that defines a contact). The new comparison is shown in Figure 13.

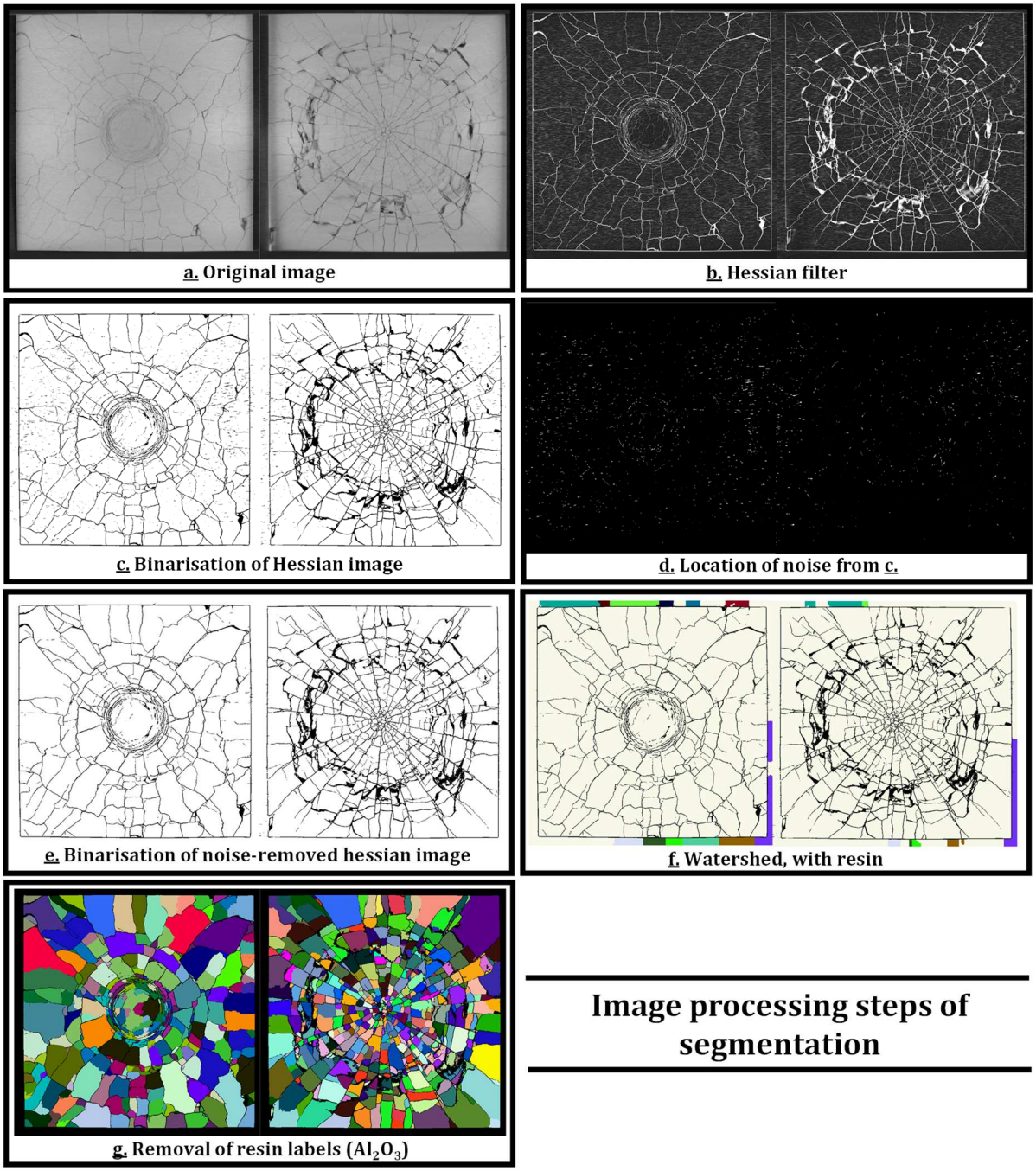

Figure 11. Processing steps of segmentation, example of Al_2O_3 ceramic target. [2-column fitting OR 1-page fitting]

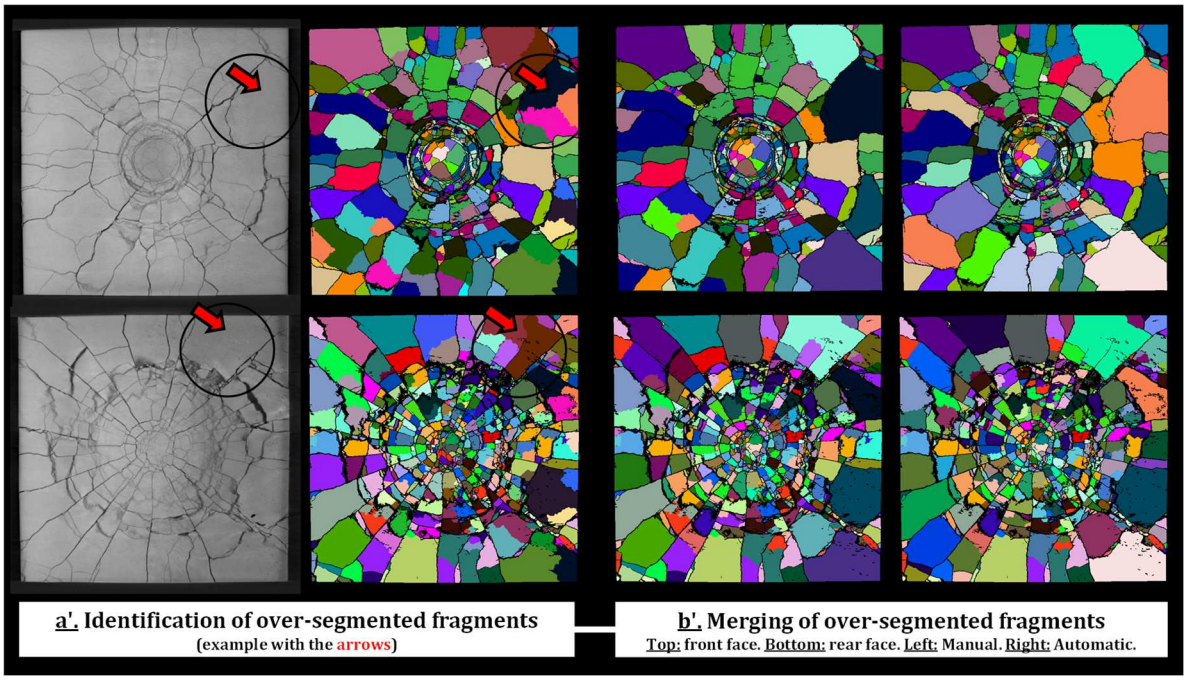

Figure 12. Comparison between tomographic and segmented images, for MAINa ceramic target. [2-column fitting]

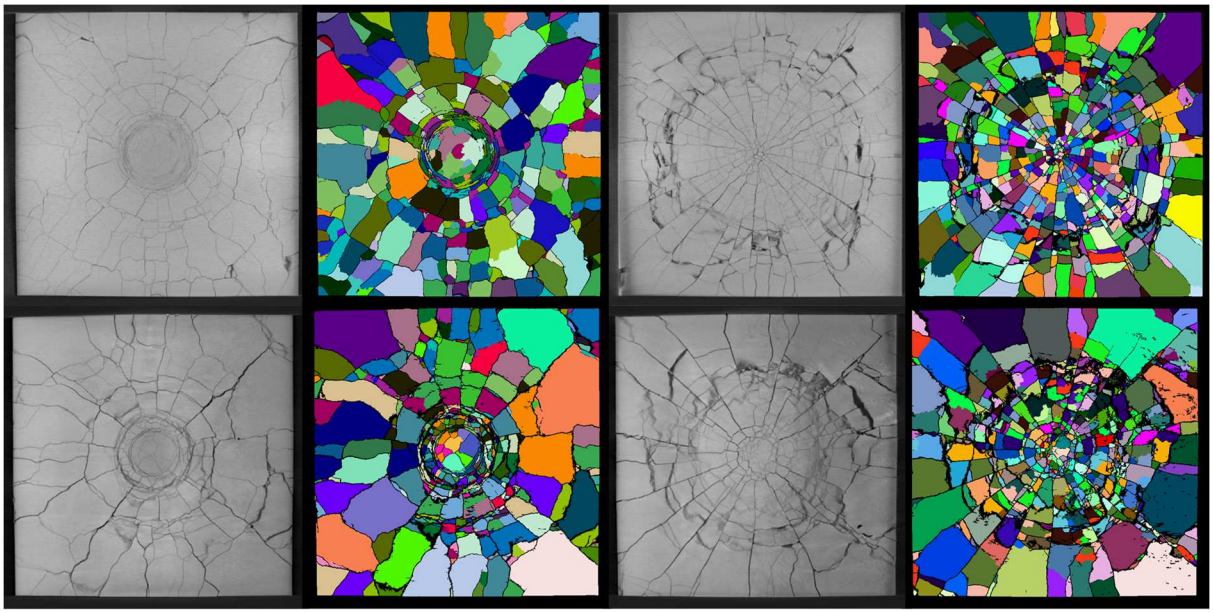

Figure 13. Final comparison between tomographic and segmented images for Al_2O_3 (top) and MAINa (bottom, automatic merging), after treating the over-segmentation of MAINa with a Python code. [2-column fitting]

Three threshold values from the hessian images were considered to investigate the influence of this parameter on the fragments distribution. As it can be seen in Figure 14 (a), the 1000 cut-off level provides too much noise to represent correctly the fragments

503 distribution. On the other hand, cut-off levels of the 1500 and 2000 lead to similar trends;
504 finally, the value 1500 was chosen. The cumulative distribution of fragments, classified by
505 ascending size just as sieving as illustrated in Figure 14 (b), gives an indication on the
506 fragmentation intensity in both Al_2O_3 and MAINa ceramic tiles. In average, the fragments
507 generated in MAINa seem to be bigger than in Al_2O_3 in an appreciable way. Below 4 – 6 mm,
508 which corresponds to the fragmentation produced at the highest strain-rates (central area of
509 the target), the two curves are very closed. On the other hand, above 4 – 6 mm, which
510 corresponds to the fragments generated at the lower strain-rate (peripheral area of the target),
511 the difference can be considered as significant. Figure 14 (b) confirms the visual inspection
512 and the quantitative estimation of cracking density carried out on the tomographic images
513 (Figure 7). Indeed, the main difference between Al_2O_3 and MAINa concerns the larger
514 fragments, which can be explained by the difference of fracture-toughness between both
515 materials. This result supports the interest of MAINa in the case of multi-hit configurations.
516 Indeed, according to STANAG 4569 (edition 3) [57] (a Standardization Agreement defined
517 by the North Atlantic Treaty Organization (NATO)), in multi-hit configurations applied to
518 non-transparent armour, the second impact is located at a distance of 25 millimetres away
519 from the first impact. Conversely, in the case of single impact, the interest of MAINa would
520 still need to be confirmed.

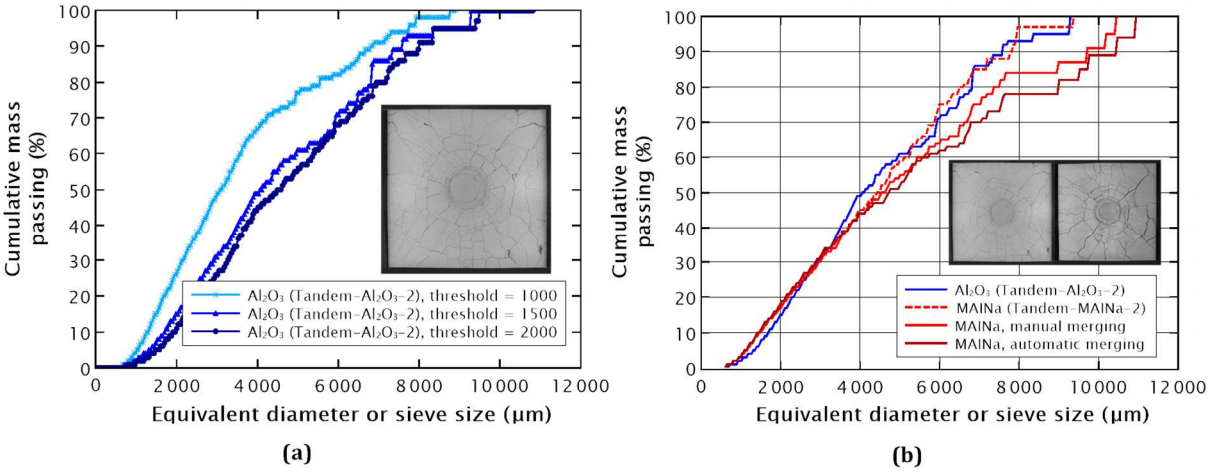

Figure 14. (a) Cumulative mass distribution of fragments as function of three values of threshold for Al_2O_3. (b) Particles mass distributions deduced from *post-mortem* tomography analysis. [2-column fitting]

Two cross sectional views (Figure 15 (a)) of the ceramics are exposed in Figure 15 (b), showing the middle part of the targets (medium slices). In the lateral views, an excess of resin at the top of each sample is noticed and corresponds to the low intensity due to the lower density of the resin compared to that of ceramics. In addition, a slight bending deformation of the fragmented ceramic plate is noted and seems to be more important in nacre-like ceramic. The most important point is that fragments in MAINa seem to be more distributed with a horizontal way (following platelets which are distributed horizontally) whereas those in Al_2O_3 seem to be more distributed along a longitudinal or inclined orientation.

(a)

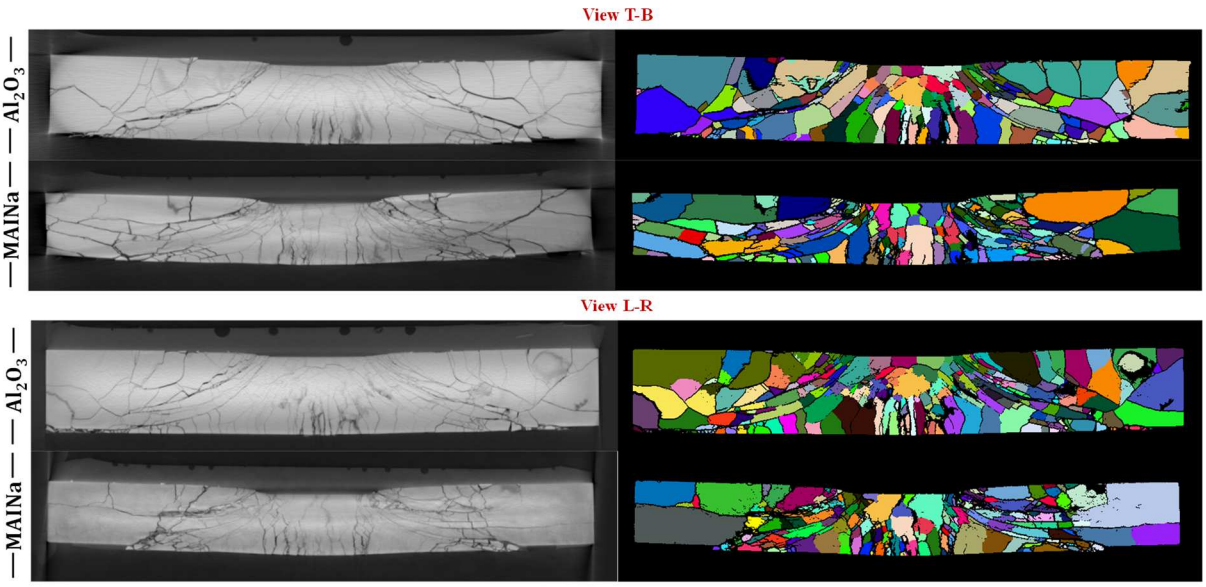

(b)

Figure 15. (a) Definition of cross-section views. (b) *Post-mortem* visualisation of two cross-section views of the Al_2O_3 and of the MAINa, from tomographic images next to their segmented images. [2-column fitting]

5. Results of penetrating impact experiment

5.1 Visualisation of fragmented ceramics subjected to penetrating impact

Several pictures captured at different times with the Kirana® ultra-high-speed camera are presented in the Figure 16. The time $t = 0$ is established when the projectile is about to reach the ceramic target although the exact position is difficult to define because of the angle of the camera. For better visualisation, the luminosity is amplified by 40% for Al_2O_3 and by 20% for both MAINa samples. The tilt angle of the projectile before impact is relatively small. During the first 120 microseconds of the selected time interval, the fragments around the point of impact are ejected while fragments farther from the point of impact remain in their initial position in the recording time.

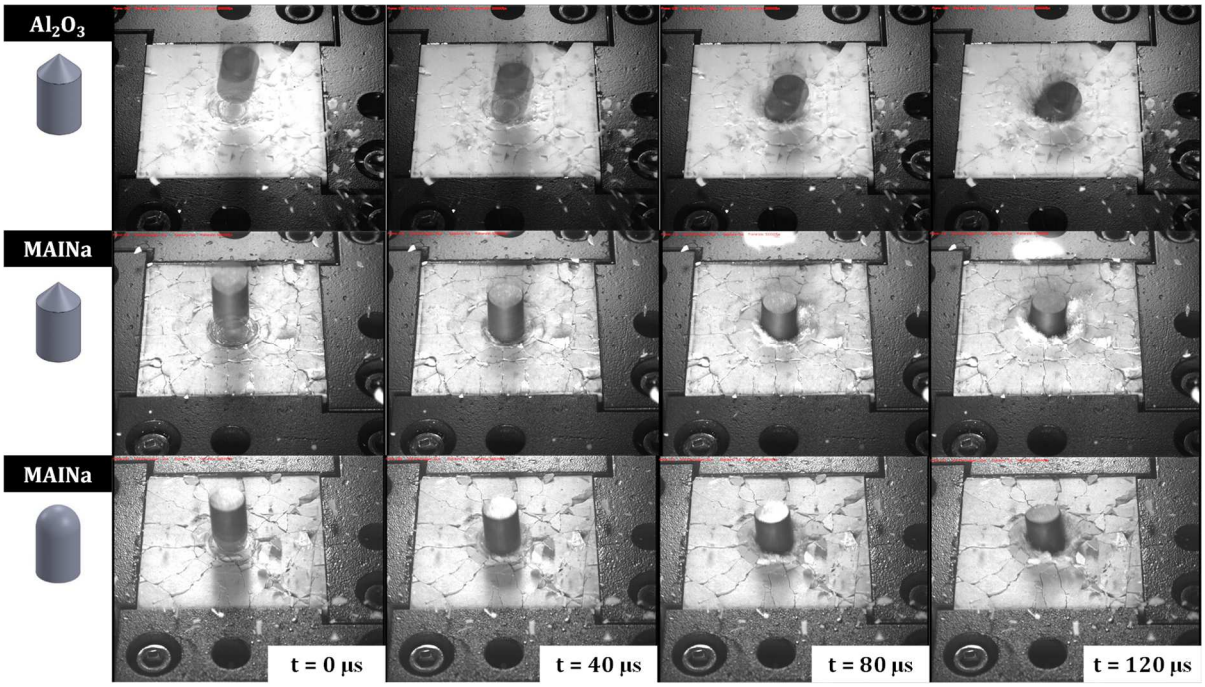

Figure 16. Penetrating test visualised with ultra-high-speed imaging at four different times, impacted at 175 m/s with the conic end projectile (Al_2O_3, MAINa) and impacted at 145 m/s with the hemispheric end projectile (MAINa). Samples, from top to bottom, are: Tandem-Al_2O_3-1, Tandem-MAINa-1b, Tandem-MAINa-1b Hemi.

[2-column fitting]

The velocity profiles measured on the rear surface of the aluminium backing are plotted for the two microstructures in Figure 17. The two tests performed with conical end projectiles show that, during the first microseconds, the increase of velocity is much faster with MAINa than in Al_2O_3 ceramic. The higher acceleration observed with MAINa, which translates into a higher initial tangent, results from a higher resistance to penetration with the nacre-like ceramic. Besides, the test performed with a hemispherical end projectile on MAINa shows a much higher amplitude of particle velocity during the first tens of microseconds of the test, which demonstrates the influence of the projectile noise shape on the penetration resisting force exerted by the projectile against the fragmented media.

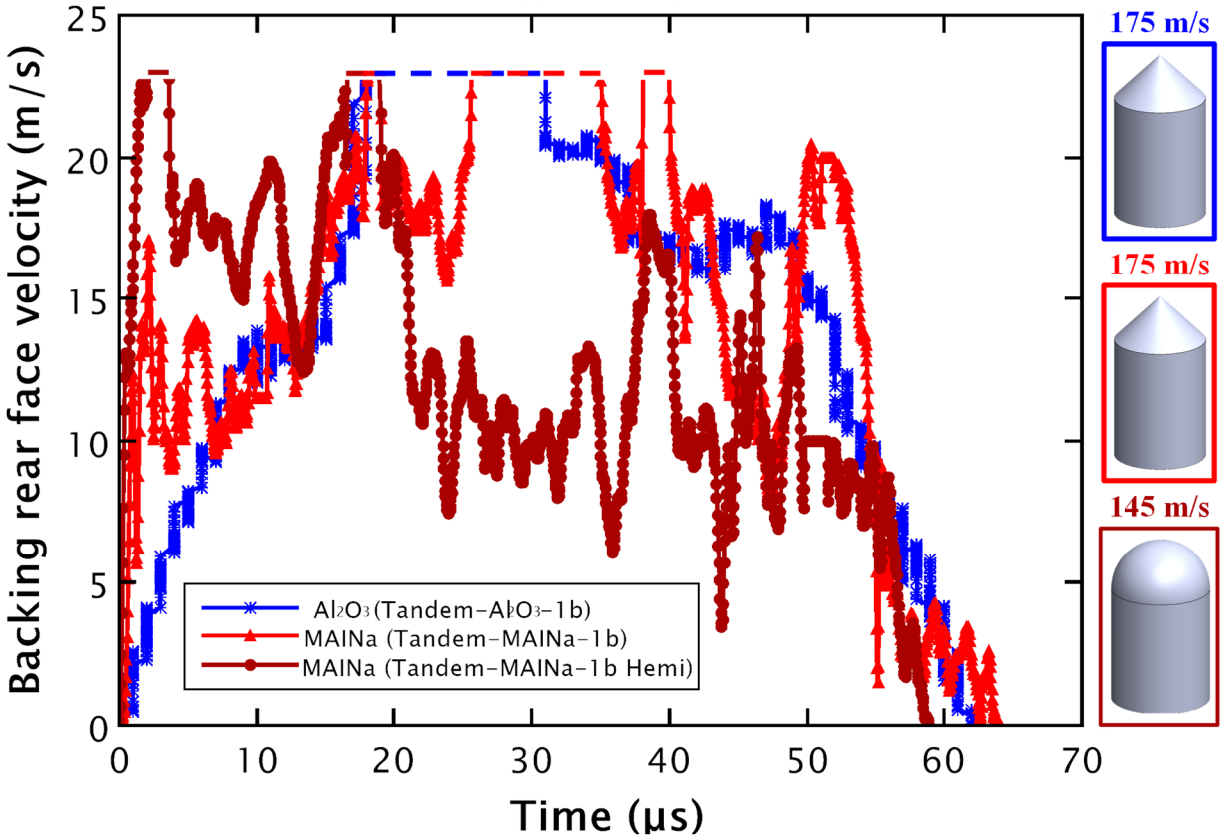

Figure 17. Free surface velocities at the rear face of the aluminium backing for the tests performed with the different alumina ceramics and the two projectile shapes. [single-column fitting]

5.2 Numerical simulation: identification of Drucker-Prager parameters

The penetrating impact, that is the second stage of tandem test, is simulated with ABAQUS. The impact velocity is set to 175 m/s (conical end impactor) and 175 and 145 m/s (hemispherical end impactor). Two symmetry conditions are considered (quarter model). These symmetry planes force the projectile on a straight penetration path, contrary to what happened in the full experiment, but this assumption can be considered as reasonably true in the considered interval of time (roughly 60 µs as projectile rotation is clearly observed only after 80 µs, *cf.* Figure 16). The mesh is made of C3D8R elements (8-node linear brick, reduced integration, hourglass control), with a mesh size of 0.25 mm for the projectile, 0.25 mm to 1.00 mm for the ceramic, 1.00 mm for the aluminium backing and 0.50 mm for the steel part. As presented in Figure 18, the meshing technique is structured for all constituents,

while for the ceramic it is structured under the projectile radius. Material parameters for the steel projectiles, the steel backing and the aluminium plate are reported in Table 4. A friction coefficient of 0.1 is applied to all surfaces in contact, using the general contact algorithm. The Figure 18 displays the geometries of the numerical model using both types of projectile. The displacement is set to zero to all nodes belonging to the bottom surface of the steel part to prevent displacement along the Y-direction ($u_y = 0$). An element control option called "distortion control" is set on the ceramic to prevent solid elements from inverting or distorting excessively. This technique is used in many analysis with large compressive and shear deformations [58]. The value of the distortion length ratio parameter, between 0 and 1, should not be high enough to not change the physical response of the material. The parameter is finally set at 0.3 *i.e.* a constraint activates as soon as an element under uniaxial compression undergoes 70% of nominal strain, thus reducing or even removing convergence issue. Upon examination of the energies provided by the explicit finite element simulations it is concluded that no major instabilities arise as the simulations progress. For instance, in the case of alumina target (Drucker-Prager model, d_0 = 80 MPa, β = 16°, ψ = 0) impacted by a conical projectile at V = 175 m/s (no tilt) it is noted that, whereas the Total Energy is keep perfectly constant during the calculation, at time T = 75 µs the Kinetic Energy tends to 0 (projectile arrest) and the Internal Energy that represents (90.4%) of the total energy is mainly composed of Inelastic Dissipated Energy (78.2%), Elastic Strain Energy (6.5%) and Artificial Strain energy (energy stored in hourglass resistances) (4.7%). Finally, at that time, Frictional Dissipated Energy represents (8.9%) and Distorsion Control Dissipation Energy is only (1.1%).

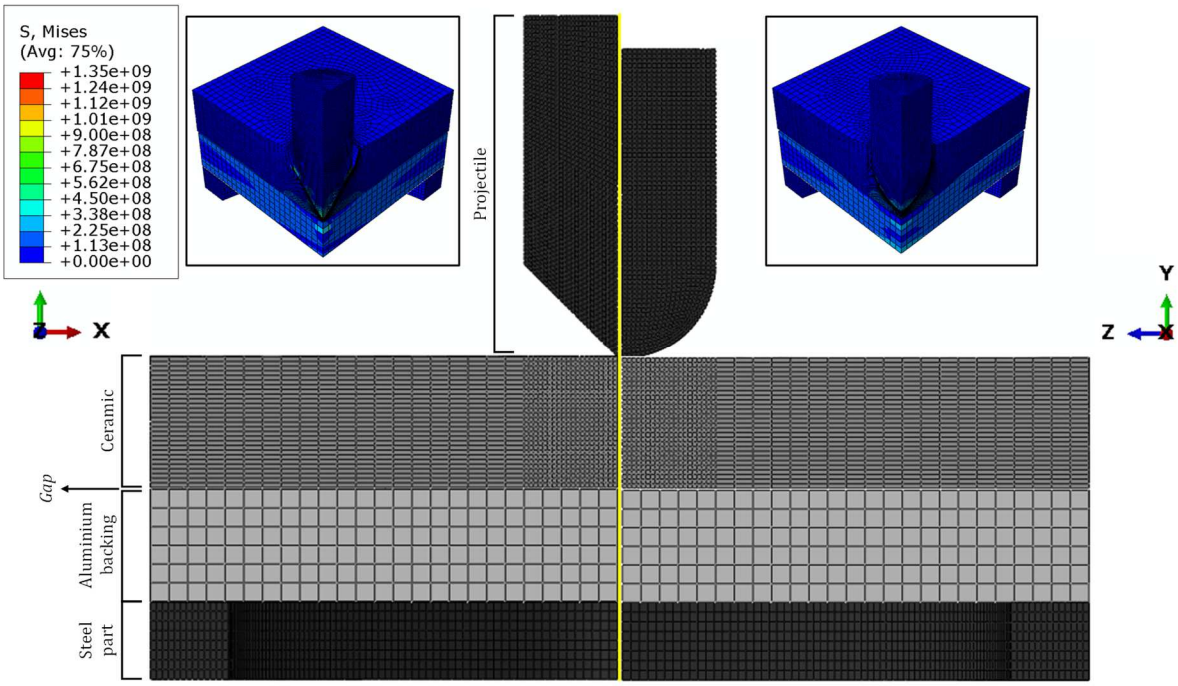

Figure 18. Numerical model of penetrating impact in tandem with both projectile shapes, with equivalent (von Mises) stress fields within Al_2O_3 impacted at 175 m/s at the end of the simulation (100 µs). [1.5-column fitting]

The constitutive model used to represent the fragmented ceramic is the Drucker-Prager (DP) model, as already employed by Zinszner [10] for simulating the response of different SiC ceramics subjected to tandem test, with the aim to identify the DP parameters (d_0, β) by inverse approach. The constitutive equation (4) describes the equivalent stress σ_{eq} as function of the pressure P in the DP model, in which the confined strength is related to the applied pressure. The parameters d_0 and β are respectively the cohesion and the (internal) friction angle of the material. d_0 is equal to the yield strength when $P = 0$, and the expression is limited to a maximum value denoted S_{max}^f for the highest pressures.

$$\sigma_{eq} = \min\left(d_0 + P.\tan(\beta), S_{max}^f\right) \quad \textbf{(4)}$$

A dilation angle ψ is also defined to represent the volume increase during shear deformation. The DP model with no dilation ($\psi = 0$) is employed in the present study. The DP constant parameters for the studied SiC (Hexoloy SA®) are $d_0 = 35\ MPa$ and $\beta = 30°$. The identification technique is the following: β is first set to 30° and d_0 is changed to obtain

612 an appropriate velocity profile that best matches to the experimental data. Then, the d_0 is fix
613 and different β are tested until the best fit is obtained. Nonetheless, as mentioned in the
614 introduction, the parameter β may not be unique and its determination might be addressed by
615 a heuristic approach. For an impact velocity established at 175 m/s, the hydrostatic pressures
616 obtained numerically is about 475 MPa in fragmented Al_2O_3 and 745 MPa in fragmented
617 MAINa with conical end projectile and below 225 MPa (Al_2O_3) and 250 MPa (MAINa) with
618 hemispherical end projectile. The numerical input parameters considered in the DP model are
619 indicated in Table 5. The Figure 19 illustrates the identification strategy with different
620 numerical curves considering various parameters of DP model, along with a comparison
621 between experimental and numerical results for both ceramics. The numerical simulations
622 support the experimental findings. Nonetheless, since the identification relies on an inverse
623 approach, this methodology with tandem is restricted to the considered Drucker-Prager model
624 which proposes a linear increase of strength with pressure.

Material	**Plasticity**		**Hardening behaviour type**	**Flow stress ratio**	$\boldsymbol{\beta}$ (°)	$\boldsymbol{\psi}$ (°)
	$\boldsymbol{d_0}$ **(MPa)**	$\boldsymbol{\varepsilon_p}$ **(%)**		$\boldsymbol{\sigma^*_{flow}}$ **(-)**		
Ceramic (Al_2O_3 and MAINa)	*To identify*	0	Shear	1	*To identify*	0

625 **Table 5.** Parameters of Drucker-Prager model used in ABAQUS (the density and elastic parameters of each
626 material are provided in Table 1 and 2, respectively).

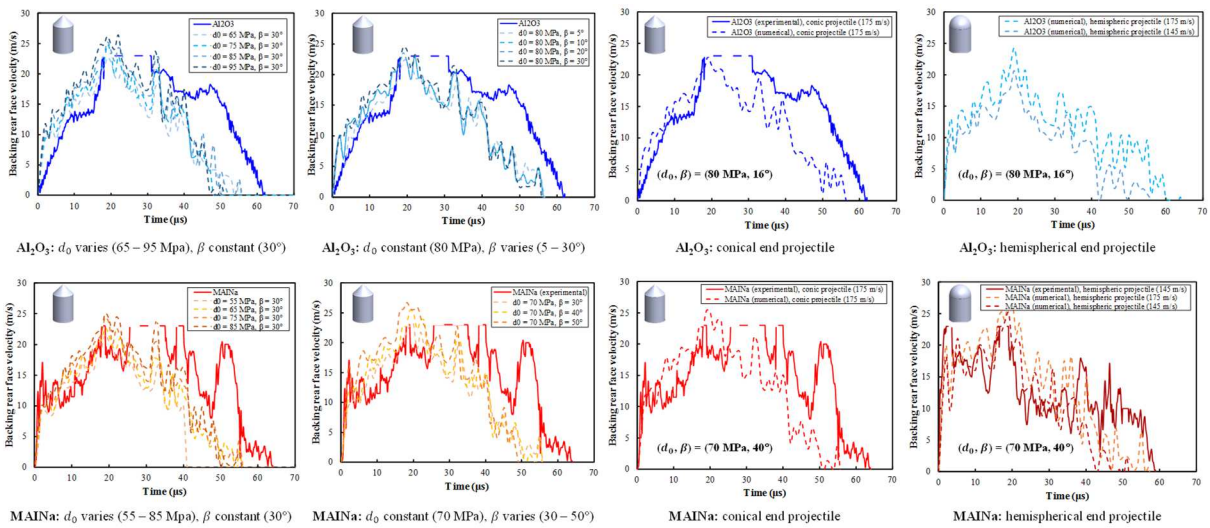

Figure 19. Identification of Drucker-Prager model parameters and validation by comparison with experimental results. [2-column fitting]

The identification of a single set of d_0 and β parameters remains delicate. However, the following parameters seem to be consistent: d_0 ~ 65 – 95 MPa for Al_2O_3 and ~ 55 – 85 MPa for MAINa; β ~ 5 – 30° for Al_2O_3 and 30 – 50° for MAINa. Further numerical simulations were led to assess the influence of the tilt angle of the projectile, up to 10° with conical projectile, assuming that tilt angle did not exceed 10° in the tests. This, to verify if the previous statement, according to which the projectile rotation observed in the Figure 16 has no influence on the identification of DP model parameters, is valid. The numerical results, depicted in Figure 20, strengthen the fact that the tilt angle has a minor effect, at least as long as it does not exceed 10°. In conclusion, the different initial slopes on the rear face velocity profiles cannot be only due to a substantial tilt of the projectile.

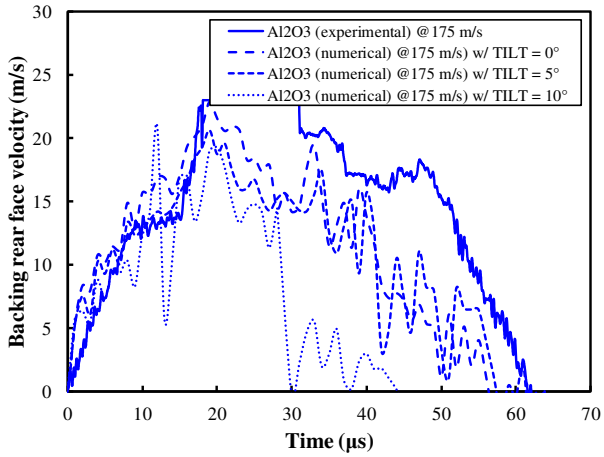

(a)

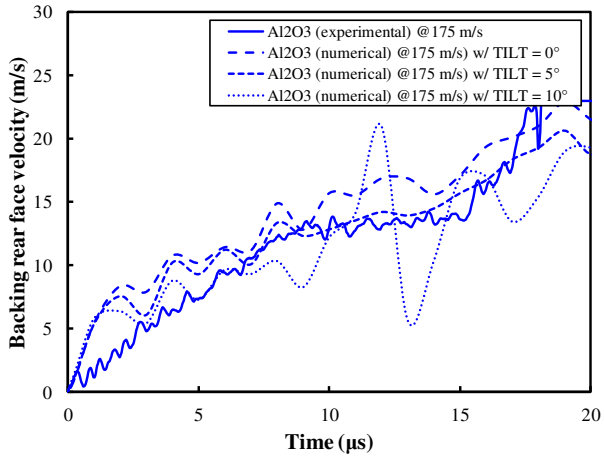

(b)

Figure 20. Numerical particle velocity at the rear face of the aluminium backing, compared to experimental data, considering the impact of a conical projectile against a fragmented alumina without tilt or with tilt angles of 5° and 10°. Results are shown (a) from 0 to 70 µs and (b) from 0 to 20 µs. [single-column fitting]

In comparison with the identification proposed by Zinszner's [10], it can be remarked that:

- d_0 for both alumina (Al_2O_3 and MAINa) materials is seen to be higher than in [10] so both fragmented alumina materials seem to be more resistant to penetration compared to a fragmented SiC.

- Secondly: the identified friction angle β of both alumina ceramics is higher with MAINa than in [10], and lower with Al_2O_3, as illustrated in Figure 17 compared to Figure 1 (c).

The Drucker-Prager plasticity yield strength for Hexoloy (SA® grade), Al_2O_3 and MAINa can be compared in Figure 21.

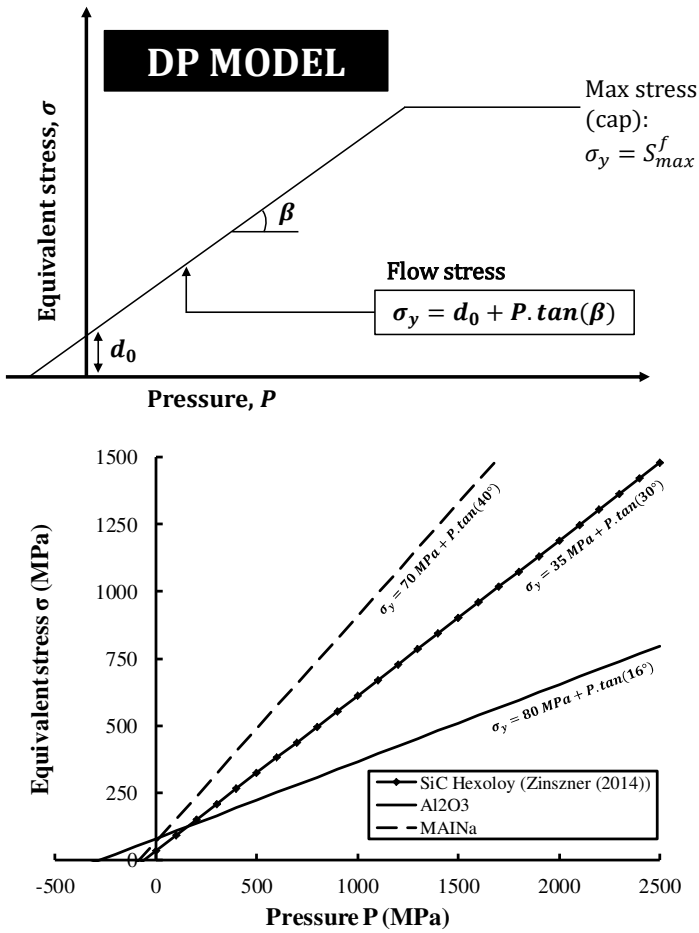

Figure 21. Description of DP model in terms of strength, with plot using the DP parameters (d_0 and β) for three materials. [single-column fitting]

The explanation of why MAINa provides better performances in tandem test than Al_2O_3 and Hexoloy SA® SiC may be attributed to the fragments size shape and orientation just beneath the impact area of normal impact. As illustrated in Figure 15, Al_2O_3 fragments are smaller beneath the projectile contact surface and more vertical so they can be more easily displaced during the penetrating impact.

663 5.3 Fragments size analysis by sieving

664 Finally, next to the second impact, the fragments of each ceramic are recovered for
665 further analysis using a dynamic microscopic analyser (equipment: ANALYSETTE 28®
666 ImageSizer from FRITSCH) for sieving. The fragments are poured on a metallic rail that
667 vibrates at a certain frequency. Fragments fall within a measurement chamber, between a
668 camera and a LED (Light-Emitting Diode) stroboscope, towards a collecting vessel.
669 Additionally, thanks to the camera, interesting information can be extracted such as: aspect
670 ratio, circularity or convexity. The distribution of fragments is reported in Figure 22 (a). First,
671 it is observed that fragments impacted at 145 m/s with hemispherical end projectile are
672 slightly larger than those impacted at 175 m/s with conic-end projectile (comparison between
673 samples "Tandem-MAINa-1b" and "Tandem-MAINa-1b Hemi"). It can be supposed that the
674 conic-end projectile, impacting at higher impact speed than the hemispherical-end projectile,
675 might have slightly changed the fragments size distribution near the impact point. In addition,
676 whereas the distribution of fragments in "Tandem-Al_2O_3-1b" after penetrating impact is
677 similar to the one obtained in "Normal-Al_2O_3-2" from tomography (Figure 14 (b)) measured
678 next to normal impact, the fragments size distribution seems to be changed with MAINa.
679 Indeed, smaller fragments are noted in "Tandem-MAINa-1b" than in "Normal-MAINa-2".
680 Indeed, while smaller fragments were observed from tomography with MAINa compared to
681 Al_2O_3, it is the opposite next to penetrating impact. It would suggest that a part of MAINa
682 fragments would be crushed during the penetrating impact, due to the higher stresses
683 supported by MAINa fragments during the second impact. The standard deviation is also
684 reported in the curves of Figure 22 (a), the fragments of MAINa remain larger than the
685 fragments of Al_2O_3, even if the gap is within the margin of error and the trend should be
686 confirmed. Furthermore, the Figure 22 (b) reveals the aspect ratio AV_F of the fragments,
687 which is the ratio between the maximum (Feret) diameter to the minimum (Feret) diameter

(the standard deviation is not reported as it tends to zero), from which two conclusions can be drawn. First, the AV_F of MAINa is nearly the same whatever the impact velocity (175 or 145 m/s) and projectile shapes used in penetrating impact, which tends to demonstrate that the size and shape of fragments remained unchanged before and after the second impact. Second, the AV_F of MAINa is overall smaller than that of Al_2O_3, which means that the fragments of MAINa are more elongated than those of Al_2O_3 (because when AV_F tends to 1, the fragment tends to be circular). This difference in fragments shape is supposed to explain the higher strength of MAINa under penetrating impact test.

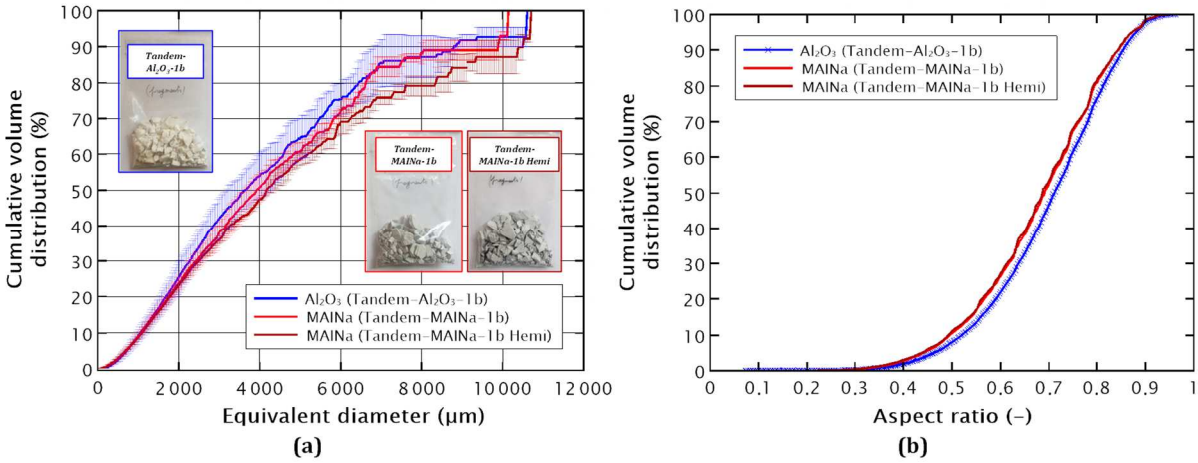

Figure 22. (a) Fragments distribution in terms of cumulative volume as function of the equivalent diameter. (b) Aspect ratio of the fragments after the second impact. [2-column fitting]

6 Conclusion

Two ceramic microstructures, a conventional alumina (Al_2O_3) and a nacre-like alumina (MAINa), are compared in terms of dynamic fragmentation under impact. The nacre-alumina ceramic is a BM material conferring improved toughening mechanisms. The cracking behaviour of both materials is investigated by means of tandem impact experiments and micro-computed tomographic analysis. The tandem impact configuration consists in a first impact of a flat-end projectile against the ceramic plate sandwiched between a steel sheet and an aluminium backing. This test produces an intense fragmentation of the ceramic plate while

keeping the fragments in place. The second impact is a penetrating impact against the fragmented ceramic backed with the aluminium plate. A numerical simulation using the Drucker-Prager model is employed to identify the plasticity parameters of the model based on the experimental backing rear face velocity captured after the second impact of tandem test.

The fragmentation pattern of the ceramic plates was analysed after the normal impact through a tomography scan. The cracking density of MAINa is estimated to be lower than the cracking density of Al_2O_3 by a factor that can go around 2 and 3. The fragments size analysis indicates that the fragments of MAINa are slightly larger than those of Al_2O_3 around the point of impact and predominantly larger far from the impact point. The farther from the impact point, the greater the difference of fragments size between the two microstructures. Thus, MAINa microstructure could be more interesting in the case of a second impact. According to the penetrating impacts, the pre-fragmented MAINa clearly appears more resistant than Al_2O_3, which suggests that the fragmentation pattern of MAINa could play an important role on its penetration strength during impact when the ceramic is already fragmented. Based on a numerical approach, in average, the following Drucker-Prager parameters identified are: (d_0 ~ 80 MPa, β ~ 16°) for Al_2O_3 and (d_0 ~ 70 MPa, β ~ 40°) for MAINa.

According to tomographic analysis and additional observations (SEM, dynamic microscopic analyser), the difference of fragmented behaviour between both materials results from a combined effect of a difference in fragments size, fragments orientation and fragments anisotropy. Indeed, compared to Al_2O_3, MAINa fragments are larger, horizontally oriented (they follow the platelets orientation) and more anisotropic (aspect ratio of fragments shape diverges from 1).

Acknowledgements

Special thanks are given to the following individuals. From 3SR laboratory: Dr. Edward Andò (research engineer) for the development of the three-dimensional segmentation algorithm and the hessian approach, and Mr. Pascal Charrier (design engineer) for his contribution in performing the tomographic scans. From CEA/DAM[1]: Dr. Jean-Luc Zinszner (research scientist) for his help and his guidance in using the Drucker-Prager model for tandem simulation. From Saint-Gobain Research Provence centre[2]: Dr. Alexane Margossian, Dr. Matthieu Graveleau and Dr. Giovanni Massasso (Research and Development engineers). From DGA[3]: Dr. François Barthélemy (design engineer). A grateful acknowledgement is handed to the DGA for co-supporting this work and to Saint-Gobain for providing the ceramic samples.

[1] CEA/DAM (French alternative energies and Atomic Energy Commission / Military Applications Division), 46500 Gramat, France. In French: *Commissariat à l'Énergie Atomique et aux énergies alternatives / Division des Applications Militaires*.

[2] Saint-Gobain Research Provence, *ex*-Saint-Gobain CREE (European Centre for Research and Study) / CNRS (French National Centre for Scientific Research), 84300 Cavaillon, France. In French: *Saint-Gobain Recherche Provence, ex-Centre de Recherches et d'Études Européen / Centre National de la Recherche Scientifique*.

[3] DGA (Directorate General of Armaments), French ministry of the Armed forces, TT (Terrestrial Technologies), 18021 Bourges, France. In French: *Direction Générale de l'Armement, ministère des Armées, Techniques Terrestres*.

Funding

This work was supported by the UGA (*Université Grenoble Alpes*) and the DGA (*Direction Générale de l'Armement*, French Government Defence procurement and technology agency), with sponsoring of Saint-Gobain.

Declaration of interest

The authors declare no conflict of interest and they have no known competing financial interests or personal relationships that could have appeared to influence the work reported in this paper.

References

[1] Barron ER, Alesi AL, Park AF. Body armor for aircrewmen. Army Natick Labs Ma Clothing and Personal Life Support Equipment Lab; 1969.

[2] McCauley JW, Crowson A, Gooch Jr. WA, Rajendran AM, Bless JB, Logan KV, et al., editors. Ceramic Armor Materials by Design: proceedings of the Ceramic Armor Materials by Design (symposium held at the Pac Rim IV International Conference on Advanced Ceramics and Glass, November 4-8, 2001 in Wailea, Maui, Hawaii). Westerville, Ohio: American Ceramic Society; 2002.

[3] Den Reijer PC. Impact on Ceramic Faced Armours. PhD thesis. Delft University of Technology (Technische Universiteit Delft), 1991.

[4] Gooch Jr. WA. An Overview of Ceramic Armor Applications (ceramic armor development). In: McCauley JW, editor. Ceram. Armor Mater. Des., Westerville, Ohio: The American Ceramic Society; 2002, p. 3–23.

[5] Normandia M, LaSalvia J, Gooch W, McCauley JW, Rajendran AM. Protecting the Future Force: Ceramics Research Leads to Improved Armor Performance. AMPTIAC Adv Mater Process Technol Inf Anal Cent 2004;8.

[6] Crouch IG. Body armour – New materials, new systems. Def Technol 2019;15:241–53. https://doi.org/10.1016/j.dt.2019.02.002.

[7] Mayseless M, Goldsmith W, Virostek SP, Finnegan SA. Impact on Ceramic Targets. J Appl Mech 1987;54:373–8. https://doi.org/10.1115/1.3173022.

[8] Malaise F. Réponse d'une céramique à l'impact d'un barreau à grande vitesse (1500 m/s). Croisement essais dynamiques-modelisation numérique. PhD thesis. École Normale Supérieure d'Arts et Métiers, 1999.

[9] Forquin P. Endommagement et fissuration de matériaux fragiles sous impact balistique - Rôle de la microstructure. PhD thesis. ENS Cachan, 2003.

[10] Zinszner J-L. Identification des paramètres matériau gouvernant les performances de céramiques à blindage. PhD thesis. Université de Lorraine, 2014.

[11] Cosculluela A. Plasticité, endommagements et ruptures des alumines soussollicitations dynamiques triaxiales : influence de la taille de grains. PhD thesis. Université de Bordeaux I, 1992.

[12] Woodward RL, O'Donnell RG, Baxter BJ, Nicol B, Pattie SD. Energy absorption in the failure of ceramic composite armours. Materials Forum 13, 174e181. Mater Forum Rushcutters Bay 1989;13:174–81.

[13] Rossiquet G. Carbure de Silicium pour Application Blindage : Élaboration et Étude du Comportement à l'Impact. PhD thesis. Université de Bourgogne & Saint-Gobain CREE, 2012.

[14] Zinszner J-L, Forquin P, Rossiquet G. Design of an experimental configuration for studying the dynamic fragmentation of ceramics under impact. Eur Phys J Spec Top 2012;206:107–15. https://doi.org/10.1140/epjst/e2012-01592-4.

[15] Zinszner JL, Forquin P, Rossiquet G. Experimental and numerical analysis of the dynamic fragmentation in a SiC ceramic under impact. Int J Impact Eng 2015;76:9–19. https://doi.org/10.1016/j.ijimpeng.2014.07.007.

[16] Forquin P, Rossiquet G, Zinszner J-L, Erzar B. Microstructure influence on the fragmentation properties of dense silicon carbides under impact. Mech Mater 2018;123:59–76. https://doi.org/10.1016/j.mechmat.2018.03.007.

[17] Forquin P, Andò E. Application of microtomography and image analysis to the quantification of fragmentation in ceramics after impact loading. Philos Trans R Soc Math Phys Eng Sci 2017;375:20160166. https://doi.org/10.1098/rsta.2016.0166.

[18] Drucker DC, Prager W. Soil mechanics and plastic analysis or limit design. Q Appl Math 1952;10:157–165.

[19] Anderson Jr. CE. A Review of Computational Ceramic Armor Modeling. In: Prokurat L, Wereszczak A, Lara-Curzio E, editors. Ceram. Eng. Sci. Proc., vol. 27, Hoboken, NJ, USA: John Wiley & Sons, Inc.; 2007, p. 1–18. https://doi.org/10.1002/9780470291368.ch1.

[20] Wilkins ML. Third Progress Report of Light Armor Program. Tech Rep UCRL-50460 Lawrence Livermore Natl Lab 1968.

[21] Wilkins ML. Fourth Progress Report of Light Armor Program. Tech Rep UCRL-50694 Lawrence Livermore Natl Lab 1969.

[22] Anderson Jr. CE, Chocron S, Behner T. A Constitutive Model for *In Situ* Comminuted Silicon Carbide. J Am Ceram Soc 2009;92:1280–6. https://doi.org/10.1111/j.1551-2916.2009.02988.x.

[23] Anderson Jr. CE, Behner T, Holmquist TJ, Orphal DL. Penetration response of silicon carbide as a function of impact velocity. Int J Impact Eng 2011;38:892–9. https://doi.org/10.1016/j.ijimpeng.2011.06.002.

[24] Forquin P, Tran L, Louvigné P-F, Rota L, Hild F. Effect of aluminum reinforcement on the dynamic fragmentation of SiC ceramics. Int J Impact Eng 2003;28:1061–76. https://doi.org/10.1016/S0734-743X(03)00034-4.

[25] Chen P-Y, Lin AYM, Lin Y-S, Seki Y, Stokes AG, Peyras J, et al. Structure and mechanical properties of selected biological materials. J Mech Behav Biomed Mater 2008;1:208–26. https://doi.org/10.1016/j.jmbbm.2008.02.003.

[26] Nakahara H, Bevelander G, Kakei M. Electron Microscopic and Amino Acid Studies on the Outer and Inner Shell Layers of *Haliotis rufescens*. Venus Jpn J Malacol 1982;41:33–46. https://doi.org/10.18941/venusjjm.41.1_33.

[27] Jackson AP, Vincent JF, Turner RM. The mechanical design of nacre. Proc R Soc Lond B Biol Sci 1988;234:415–440.

[28] Bertoldi K, Bigoni D, Drugan WJ. Nacre: An orthotropic and bimodular elastic material. Compos Sci Technol 2008;68:1363–75. https://doi.org/10.1016/j.compscitech.2007.11.016.

[29] Menig R, Meyers MH, Meyers MA, Vecchio KS. Quasi-static and dynamic mechanical response of Haliotis rufescens (abalone) shells. Acta Mater 2000;48:2383–2398.

[30] Radi K, Jauffrès D, Deville S, Martin CL. Elasticity and fracture of brick and mortar materials using discrete element simulations. J Mech Phys Solids 2019;126:101–16. https://doi.org/10.1016/j.jmps.2019.02.009.

[31] Wat A, Lee JI, Ryu CW, Gludovatz B, Kim J, Tomsia AP, et al. Bioinspired nacre-like alumina with a bulk-metallic glass-forming alloy as a compliant phase. Nat Commun 2019;10. https://doi.org/10.1038/s41467-019-08753-6.

[32] Mayer G. New toughening concepts for ceramic composites from rigid natural materials. J Mech Behav Biomed Mater 2011;4:670–81. https://doi.org/10.1016/j.jmbbm.2010.08.001.

[33] Khayer Dastjerdi A, Rabiei R, Barthelat F. The weak interfaces within tough natural composites: Experiments on three types of nacre. J Mech Behav Biomed Mater 2013;19:50–60. https://doi.org/10.1016/j.jmbbm.2012.09.004.

[34] Niebel TP, Bouville F, Kokkinis D, Studart AR. Role of the polymer phase in the mechanics of nacre-like composites. J Mech Phys Solids 2016;96:133–46. https://doi.org/10.1016/j.jmps.2016.06.011.

[35] Aoyanagi Y, Okumura K. Toughening in a nacre-like soft-hard layered structure due to weak nonlinearity in the soft layer. Phys Rev Mater 2019;3:053607.

[36] Bouville F, Maire E, Meille S, Van de Moortèle B, Stevenson AJ, Deville S. Strong, tough and stiff bioinspired ceramics from brittle constituents. Nat Mater 2014;13:508–14. https://doi.org/10.1038/nmat3915.

[37] Munch E, Launey ME, Alsem DH, Saiz E, Tomsia AP, Ritchie RO. Tough, Bio-Inspired Hybrid Materials. Science 2008;322:1516–20. https://doi.org/10.1126/science.1164865.

[38] Deville S. Ice templating of porous materials. Sylvain Deville 2011. https://sylvaindeville.net/research/ice-templating-of-porous-materials/ (accessed January 14, 2020).

[39] Deville S. The lure of ice-templating: Recent trends and opportunities for porous materials. Scr Mater 2018;147:119–24. https://doi.org/10.1016/j.scriptamat.2017.06.020.

[40] Deville S, Bouville F, Stevenson AJ. CERAMIC PRODUCT WITH ORIENTED PARTICLES AND METHOD FOR THE PRODUCTION THEREOF. WO 2015/189659, 2015.

[41] Grujicic M, Ramaswami S, Snipes J. Nacre-like ceramic/polymer laminated composite for use in body-armor applications. AIMS Mater Sci 2016;3:83–113. https://doi.org/10.3934/matersci.2016.1.83.

[42] Flores-Johnson EA, Shen L, Guiamatsia I, Nguyen GD. Numerical investigation of the impact behaviour of bioinspired nacre-like aluminium composite plates. Compos Sci Technol 2014;96:13–22. https://doi.org/10.1016/j.compscitech.2014.03.001.

[43] Forquin P, Savino N, Lamberson L, Barsoum M, Morais M. Dynamic Fragmentation of MAX Phase Ti3SiC2 from Edge-On Impact Experiments. In: Kimberley J, Lamberson LE, Mates S, editors. Dyn. Behav. Mater. Vol. 1, Cham: Springer International Publishing; 2019, p. 355–9. https://doi.org/10.1007/978-3-319-95089-1_65.

[44] Bernache-Assollant D, Bonnet J-P. Frittage : aspects physico-chimiques - Partie 1 : frittage en phase solide. Tech Ing 2005:AF6620.1-AF620.20.

[45] Bernache-Assollant D, Bonnet J-P. Frittage : aspects physico-chimiques - Partie 2 : frittage en phase liquide. Tech Ing 2005:AF6621.1-AF6621.14.

[46] Benameur N, His C, Leloup J. DENSE SINTERED PRODUCT. WO 2018/141736, 2018.

[47] Zirconia (Tosoh Yttria-stabilized Zirconia (YSZ)). Tosoh Adv Ceram Zirconia Powders [no date]. https://www.rbhltd.com/wp-content/uploads/2019/05/Tosoh-Zirconia-Brochure.pdf (accessed June 24, 2020).

[48] NF EN 843-4, Advanced technical ceramics - Mechanical properties of monolithic ceramics at room temperature - Part 4 : Vickers, Knoop and Rockwell superficial hardness, Afnor standard, https://www.boutique.afnor.org/standard/nf-en-843-4/advanced-technical-ceramics-mechanical-properties-of-monolithic-ceramics-at-room-temperature-part-4-vickers-knoop-and-rockwell-s/article/733432/fa103648 2005.

[49] ASTM C1259-15, Standard Test Method for Dynamic Young's Modulus, Shear Modulus, and Poisson's Ratio for Advanced Ceramics by Impulse Excitation of Vibration, ASTM International, West Conshohocken, PA, www.astm.org 2015.

[50] NF EN 843-1, Céramiques techniques avancées - Propriétés mécaniques des céramiques monolithiques à température ambiante - Partie 1 : détermination de la résistance à la flexion, Afnor Standard, https://www.boutique.afnor.org/norme/nf-en-843-1/ceramiques-techniques-avancees-proprietes-mecaniques-des-ceramiques-monolithiques-a-temperature-ambiante-partie-1-determination-/article/734585/fa122351 2007.

[51] Weibull W. A Statistical Theory of the Strength of Materials. Gen Litografiska Anst Förlag 1939;151:45.

[52] Weibull W. A Statistical Distribution Function of Wide Applicability. J Appl Mech 1951;18:293–7.

[53] Davies DGS. The statistical approach to engineering design in ceramics. Proc Br Ceram Soc 1973;22:429–52.

[54] ASTM C1421-10, Standard Test Methods for Determination of Fracture Toughness of Advanced Ceramics at Ambient Temperature, ASTM International, West Conshohocken, PA, www.astm.org 2010.

[55] Chen MW, McCauley JW, Dandekar DP, Bourne NK. Dynamic plasticity and failure of high-purity alumina under shock loading. Nat Mater 2006;5:614–8. https://doi.org/10.1038/nmat1689.

[56] Stamati O, Andò E, Roubin E, Cailletaud R, Wiebicke M, Pinzon G, et al. spam: Software for Practical Analysis of Materials. J Open Source Softw 2020;5:2286. https://doi.org/10.21105/joss.02286.

[57] Nato/PfP, Procedure for evaluating the protection level of logistic and light armoured vehicles 2005.

[58] ABAQUS - Lecture 6: Adaptive Meshing and Distortion Control. ABAQUSExplicit Adv Top 2005. https://imechanica.org/files/l6-adaptive-mesh.pdf (accessed January 20, 2020).